THESIS

LASER DIAGNOSTIC METHODS FOR PLASMA SHEATH POTENTIAL MAPPING AND ELECTRIC FIELD MEASUREMENT

Submitted by

Jordan L. Rath

Department of Mechanical Engineering

In partial fulfillment of the requirements

For the Degree of Master of Science

Colorado State University

Fort Collins, Colorado

Fall 2013

Master's Committee:

Advisor: Azer P. Yalin

John D. Williams
Jorge G. Rocca

ABSTRACT

LASER DIAGNOSTIC METHODS FOR PLASMA SHEATH POTENTIAL MAPPING AND ELECTRIC FIELD MEASUREMENT

This thesis presents the development of two laser diagnostic approaches for electric field measurements in plasmas and gases. Hall effect thrusters, and other electric propulsion devices, have limited lifetimes due to the erosion of components by ion bombardment of surfaces. A better understanding of the electric field structure in the plasma sheaths near these surfaces would enable researchers to improve thruster designs for extended lifetime and higher efficiency. The present work includes the development of a laser induced fluorescence technique employing a diode laser at 835 nm to measure spatially resolved xenon ion velocity distribution functions (IVDFs) near plasma-surface interfaces (sheaths), from which electric field and spatially-resolved potentials can be determined. The optical setup and demonstrative measurements in a low-density multi-pole plasma source are presented. Also included in this thesis is development of a cavity-enhanced polarimetry technique for electric field measurements in gases via the optical Kerr effect. The high finesse optical cavity allows sensitive measurement of the electric field induced birefringence, improving upon the detection limits of past work using related multi-pass techniques. Experimental results are presented for carbon dioxide, nitrogen, oxygen and air along with comparisons to model predictions based on published Kerr constants.

ACKNOWLEDGEMENTS

I would like to thank everyone who has played a part in the completion of this thesis. I would like to thank my advisor Dr. Azer Yalin, who provided much-needed guidance when progress was at a standstill and provided me with the opportunity to work on such interesting projects. I would like to thank Brian Lee for patiently answering the multitude of questions I have plied him with over the past 3 years and for providing invaluable guidance in every project I have undertaken at the LPDL. I would like to thank Dr. John Williams for all of his help and advice on every plasma or vacuum chamber related crisis in which I found myself. I would also like to thank the amazing graduate students that I have been able to work with during my time at the LPDL: Isaiah Franka, Randy Leach, Adam Friss and all the others who supported me in my research and provided countless sanity checks when my own common sense failed me. Finally I would like to to thank my family for the endless support and encouragement they have continuously provided.

TABLE OF CONTENTS

LIST OF FIGURES

1. INTRODUCTION

1.1 HALL THRUSTERS AND ELECTRIC PROPULSION

Electric propulsion (EP) systems have been gaining popularity in the aerospace field as a viable option for long term positioning and thrusting applications. In EP systems, thrust is generated by the electro-static acceleration of ions within induced electric fields. EP thrusters are advantageous as they reduce the amount of propellant required for a specific space mission compared to other propulsion methods [1]. Various forms of these EP thrusters have been created utilizing many different methods of ionization and electric (and magnetic) field configurations to create thrust to propel spacecraft. Although these thrusters have been around for decades, more research is required to fully understand the intricacies of their operation and ultimately to increase their lifetime.

The Hall Effect thruster (HET), in particular, shows great promise for earth orbit missions [2] and could potentially be scaled in power to propel larger spacecraft with greater thrusting needs. The HET is not as efficient as other electric propulsion methods, such as ion thrusters, but their relative simplicity can make them more desirable for many applications. The HET is a device comprised of a cylindrical channel with an anode at the base, a magnetic circuit which creates radial magnetic field lines across the channel and an external cathode. A simple schematic cross-section of a HET is shown in Figure 1. During HET operation, electrons are emitted by the external cathode and drawn into the thruster channel by the positively biased anode. An azimuthal Hall current is created as the electrons are trapped by the Lorentz force induced by their motion in the radial magnetic field. A propellant gas (typically xenon) is fed

into the channel from the base towards the trapped electrons. The electrons ionize the propellant atoms and the resulting ions are accelerated by the electric field between the positively biased anode and negatively charged electron cloud. The resulting plasma cloud of propellant ions and electrons that were not pulled into the thruster channel then begin to recombine and exits the thruster channel in the plume. This description is a very simplified explanation of the highly complex operation of the HET, which is adequate for the purposes of this thesis, but more detailed description of the operation of HETs and their design considerations is given by Goebel and Katz [1].

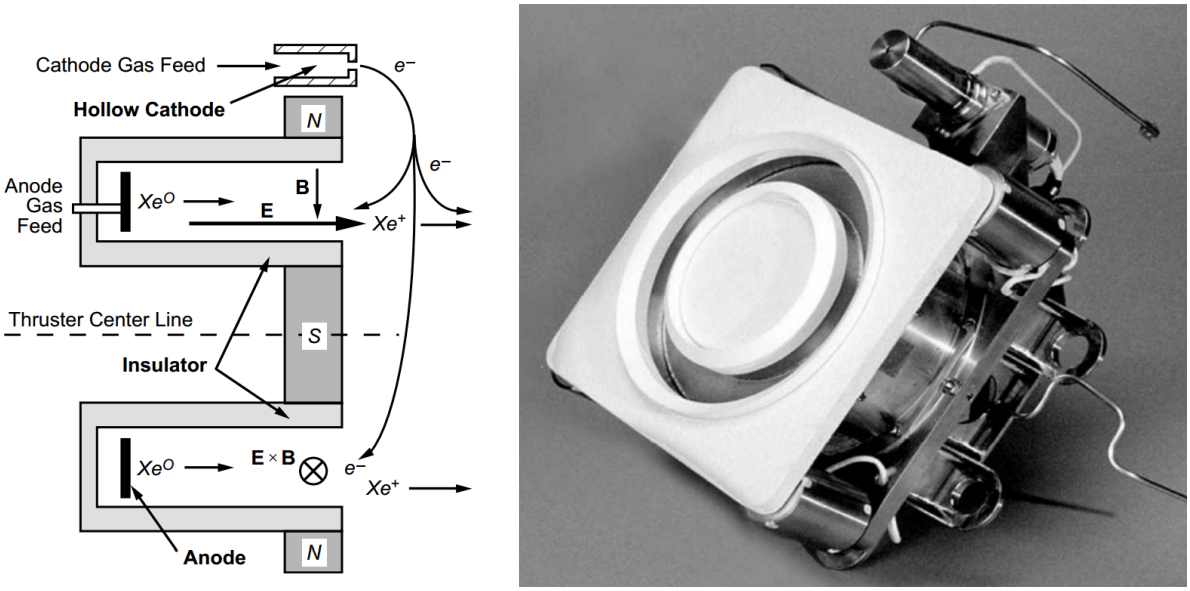

Figure 1 Left: Hall thruster cross-section schematic showing the radial magnetic field and the accelerating electric field. Right: Photograph of a BPT-4000 Hall thruster manufactured by Aerojet [1].

One of the most significant issues in HET design is the limited thruster lifetime which can preclude use in long term mission applications. HET lifetimes are limited to a large degree by plasma-wall interactions, specifically erosion of the ceramic channel walls due to sputtering by ion bombardment. As the propellant ions are accelerated towards the exit plane of the

thruster, some of the ion trajectories can include some radial components which direct the energetic ions towards the channel wall. Small amounts of the ceramic channel wall can be removed by sputtering when these ions strike the wall with high velocity, resulting in the slow erosion of the ceramic channel wall during extended operation. When the bombarding ions have eroded the channel walls to the point of exposing the magnetic circuit to the plasma, the thruster performance will typically begin to drop to the point of failure. A better understanding of the plasma-wall interactions would aid researchers in development of predictive models that would eliminate the need to perform long-duration life tests to determine failure modes and thruster lifetimes [2]. These plasma-wall interactions also influence plasma heating and electron loss, which in turn impacts the channel conductivity and thruster efficiency.

1.2 PLASMA – WALL INTERACTIONS

In the most basic terms, a plasma is a collection of charged particles with equal densities of positive ions and negative free electrons. This is typically an appropriate assumption when one is dealing with the plasma bulk, far from the physical boundaries confining the plasma, but when one begins to look at the particle dynamics near to these boundaries there are significant changes in the density balance. The changes occur as a result of the differing velocities between the electrons and ions. The ions are much more massive than the electrons and therefore, for a given energy, move much more slowly. The electrons are more mobile than the ions so (prior to charging of the wall) they provide a larger flux to the wall causing a negative charge to accumulate on the wall. The negative charge lowers the potential on the wall and attracts positive ions such that the fluxes are balanced. This process of charge balancing is known as

Debye Shielding and leads to a potential variation in a thin layer near the wall having thickness of several Debye lengths [3]. The bulk plasma far from the wall remains homogenous and charge neutral. The Debye length, and thus the sheath thickness, is determined by the electron temperature, T_e, and the bulk plasma density, n_p. The Debye length, λ_D, is found as:

$$\lambda_D \equiv \sqrt{\frac{\epsilon_0 k_B T_e}{n_p e^2}} \tag{1}$$

where ϵ_0 is the permittivity of free space, k_B is Boltzmann's constant and e is the charge of an electron. The structure and shape of the plasma potential, i.e. the plasma sheath, is influenced by many parameters [4-13].

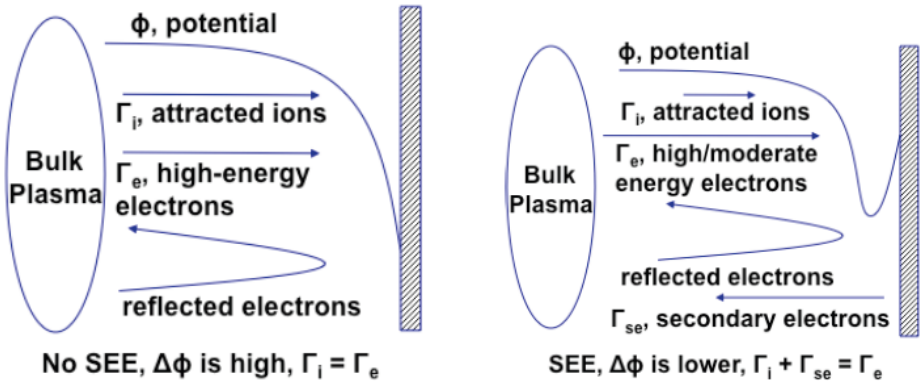

Figure 2 Sheath potential profiles with no SEE (left); and with significant SEE (right).[14]

For plasma-wall interactions in Hall thrusters, a particular interest is the effect of secondary electron (SEE) caused by ion bombardment of the ceramic wall. SEE is a heterogeneous reaction in which the bombardment of a surface results in the additional emission of electrons from that surface, typically at lower energies than that of the incident particle [12].

The emission of these lower energy secondary electrons from the wall can affect the sheath potential structure (since the charge distribution changes), plasma discharge conditions, and therefore thruster performance. The parameter that is affected most by the secondary electrons is the sheath potential between the wall and the bulk plasma. As shown in Figure 2, the various ion and electron fluxes alter the plasma potential φ including the possible formation of virtual cathodes (local potential minima) near the ceramic surface [15]. These effects depend on the ion and electron energy distributions as well as surface properties, and their influence on thruster operation remains an open question in HET studies. The present research seeks to develop a method to characterize the plasma potential distributions resulting in sheaths near ceramic surfaces representative of those used in the discharge channels of HETs.

1.3 DIAGNOSTIC TECHNIQUES FOR PLASMA STUDIES

Most plasma diagnostic testing is conducted using probe measurement techniques in which probes are inserted into a plasma and various parameters are derived from the voltage and current characteristics of the probe operation. The most widely used probe measurement technique is the interpretation of Langmuir probe traces collected by inserting an electrode of well-known dimensions into a plasma and monitoring current while varying the probe's potential. By varying the probe potential, the nature of the sheath surrounding the exposed probe surface changes to allow for negative ion current and positive electron current at low and high potentials, respectively. Using Langmuir probe theory [16] this trace of probe current versus probe potential can be used to determine many different plasma parameters including plasma potential, electron temperature, ion density, and electron density.

Emissive probes are also widely used for direct measurement of local plasma potential without the need of a voltage sweep or data processing. The emissive probe is a small filament loop on the end of an insulative ceramic tube which is electrically heated until electron emission occurs, at which point the emitted electrons neutralize the sheath around the probe tip causing the probe to float at the local plasma potential. Many other probe techniques are used to measure various plasma parameters including E×B probes that can be used to determine charge states of ions and Faraday probes to measure ion current density.

One common drawback to using these probe measurements is a general lack of spatial resolution which often precludes their use in many precise applications. Recent work [15][17] has shown successful operation of Langmuir probes with special resolution of ~1 mm and emissive probes with ~2 mm resolution. This resolution is adequate when measuring sheath potentials in plasmas with very low densities due to their long Debye length and therefore thick sheath, but measurement of sheath profiles that are much smaller (at higher plasma density) require much finer resolution than these probes will allow. Another shortcoming of probe measurements is their sensitivity to heat load in high temperature plasmas such as are seen in Hall thrusters and other electric propulsion devices. For these reasons, alternative measurement methods capable of fine spatial resolution and continuous use without failure would be preferable.

Non-intrusive plasma diagnostics typically involve the use of laser measurement techniques such as LIF or Cavity Enhanced Spectroscopy to determine properties without directly interacting with the plasma. Because these techniques do not alter the plasma properties they are often capable of very fine spatial resolution, high accuracy and long-term use. Examples of these types of diagnostics are described in the following sections.

1.3.1 SHEATH PROFILE MEASUREMENTS USING LASER INDUCED FLUORESCENCE VELOCIMETRY

Laser induced Fluorescence (LIF) studies have proven useful in measuring sheath potentials by measuring ion velocities at various points within the sheath [8, 18, 19]. In general, as the bulk plasma ions approach the wall, the negative potential accelerates the positively charged ions toward the wall. By measuring the Doppler shifted frequency at which the moving ions absorb the incident photons; one can determine the velocities of those ions and calculate the potential through which the ion was accelerated. The present research uses similar LIF methods to map the potential distributions but with emphasis on measuring the potential variations near ceramic surfaces. Further detail is provided in chapter 2.

1.3.2 ELECTRIC FIELD MEASUREMENTS VIA OPTICAL KERR EFFECT

There are few methods for non-invasive measurements of the electric field in non-radiating gases. A method which has been used with some success is based on the Kerr electro-optic effect (see for example general discussion by Buckingham and Dunmur [20]). The Kerr electro-optic effect is a change in the refractive index of a medium in the presence of an applied electric field. More specifically, the medium becomes birefringent with different refractive indices for light propagation polarized parallel versus perpendicular to the applied electric field. Accurate determination of the refractive index difference of a gas sample in the presence of an electric field allows for measurement of that electric field.

The simplest configuration one could employ for such a measurement would require linearly polarized light, oriented 45º to the applied electric field, to be directed through the electric field into a nulled polarizer (90º to incoming light polarization). In absence of any applied electric field, the output of the nulled polarizer should be near zero (based on extinction ratio of the polarizer used and the linearity of the incoming light). Any electric field-induced birefringence would cause a phase difference between the parallel and perpendicular polarization components and thus induce ellipticity in the polarization of the incoming light, resulting in increased optical power exiting the nulled polarizer. The magnitude of this birefringence, however, is very small and therefore extremely difficult to detect unless very strong electric fields are being used or the phase difference is allowed to accumulate over a very long path length through the electric field. Multi pass cell designs have been used in the past to extend the optical path length of such measurements [20], to enable electric field measurements in physically smaller electric fields and to increase the overall sensitivity of such measurements in weaker electric fields. Further detail on Kerr effect theory and past work is given in section 3.1.

1.4 THESIS OBJECTIVES

Non-intrusive laser diagnostic techniques for measurements in plasmas and gases provide many advantages over other conventional methods especially in the field of electric propulsion and plasma studies. Detailed study of Hall thruster operation, particularly plasma/material interactions, is crucial to the advancement of the technology. Development of diagnostic techniques that are more accurate and capable of much finer spatial resolution will facilitate this research and propel the technology toward increases in thruster efficiencies and lifetimes.

This thesis concerns the development of two laser diagnostic techniques for sheath potential mapping in low density plasmas and electric field measurements in gases:

- Laser induced fluorescence velocimetry of xenon ions in plasma sheaths for spatially resolved potential mapping. Description of the plasma source and other instrumentation as well as development of LIF procedure including frequency monitoring, fluorescence collection and optical noise filtering are presented. Also discussed is work specific to absolute wavelength reference determination using an opto-galvanic cell and optimization of Lock-In Amplifier settings for maximum noise reduction. Finally an optical study to determine sensitivity limits of the system with some preliminary Doppler shift measurements taken with the current LIF setup are provided.
- Cavity enhanced polarimetry for electric field measurement in gases. Kerr Effect theory and its application to electric field measurements is discussed along with description of the instrumentation used to observe Kerr induced phase shifts in temporal traces of cavity resonances. Experimental results for electric field measurements in various gases are also presented with discussion of sensitivity and detection limits.

Chapter 2 includes a description of the Sheath potential mapping LIF measurement technique and instrumentation as well as work discussion of factors that limit the measurement sensitivity. Chapter 3 will discuss the development of a cavity enhanced polarimetry instrument which will include a description of the instrument and its performance using various gases. Finally Chapter 4 will conclude the thesis and discuss future improvements to both measurement techniques.

2. LASER INDUCED FLUORESCENCE VELOCIMETRY FOR MEASUREMENT OF ION VELOCITY DISTRIBUTION FUNCTIONS NEAR CERAMIC SURFACES

2.1 MEASUREMENT TECHNIQUE AND INSTRUMENTATION

The LIF scheme used in this research takes advantage of the singly ionized xenon excitation transition from the $5d[4]_{7/2}$ energy level to the $6p[3]_{5/2}$ level, which corresponds to an absorption wavelength of 834.954 nm (vacuum). Once the ion is excited by an incoming photon of that wavelength, the ion then relaxes to the $6s[2]_{3/2}$ energy level, emitting a 542 nm wavelength photon via spontaneous emission. This type of non-resonant spectroscopic scheme is ideal for noise reduction in LIF systems, since it allows for the interrogating beam to be easily distinguished from the fluoresced light using a monochromator or other wavelength dependent optical filtering device.

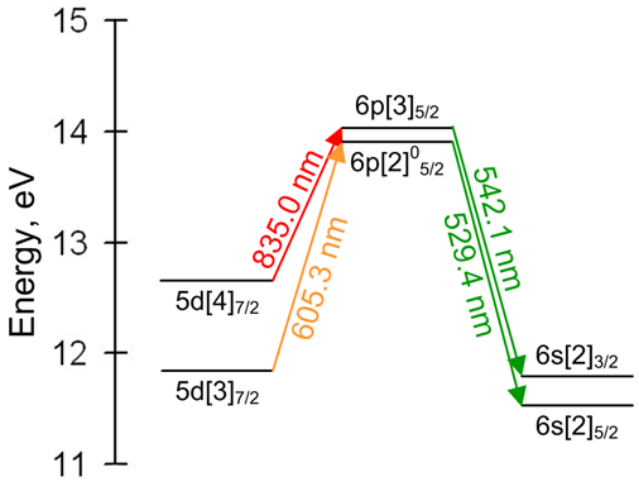

Figure 3 Spectroscopic scheme with energy levels. [7]

Xenon ions within a plasma have a certain velocity distribution resulting from the random movement and collisions that occur within the fluid-like plasma bulk. When an interrogating light source injects photons into the plasma along one defined axis, the particle's movement of the absorbing ion (relative to the laser beam) causes the absorbing ions to observe the incoming photons at a shifted frequency. This Doppler shifting of the absorption transition frequency thereby allows measurement of the ion velocity distribution function (IVDF). The IVDF is found by recording the fluorescence strength while varying the wavelength of the interrogating light source across the shifted and broadened frequency spectrum. The laser frequency at which the ion absorbed and subsequently fluoresced light can then be converted into the velocity of the absorbing ion [8]:

$$v_z = \frac{c\Delta\nu}{\nu_0 + \Delta\nu} \approx \frac{c\Delta\nu}{\nu_0} = \lambda_0 \Delta\nu \tag{2}$$

where v_z is ion velocity in the direction of the laser wave vector, c is the speed of light, $\Delta\nu$ is the Doppler shift (frequency in GHz), ν_0 is the absorption transition center frequency, and λ_0 is the absorption transition center wavelength. Observing the fluoresced light from only a small section of the beam path can then provide information as to the velocity distribution of the ions within that finite collection volume and thus enable spatially resolved measurement of local ion velocities. The resulting spectrum is also by broadened by hyperfine structure but, for the transition studied here, the hyperfine width is relatively small (~450 MHz)[7].

As discussed in section 1.1, variations in plasma potential within the sheath accelerate the ions towards the negatively charged wall, thereby changing the IVDFs at different positions near the wall. Analysis of the changes in the spatially resolved IVDF then allows for recovery of the

spatial distribution of plasma potential [8], i.e. "mapping the sheath." The simplest interpretation is through a conservation of energy balance of the ion's kinetic energy and the acceleration due to the plasma potential [3]:

$$\frac{1}{2}m_i v_z(z)^2 = \frac{1}{2}m_i {u_B}^2 - e\phi(z) \tag{3}$$

Where m_i is the mass of the ion, *u(z)* is the velocity of the ion as a function of *z*, *z* is the distance from the wall, u_B is the resulting Bohm velocity, *e* is the electron charge and $\phi(z)$ is the plasma potential. Plasma potential is then found as:

$$\phi(z) = \frac{m_i}{2e}(u(z)^2 - {u_B}^2) \tag{4}$$

2.1.1 PLASMA SOURCE APPARATUS

The plasma discharge source used in this study was designed and fabricated by researchers at the University of Michigan specifically for the purpose of this research. The source was designed to create low-density plasmas with relatively thick sheaths amenable to spatially resolved LIF studies. The plasma discharge source uses a tungsten filament as an electron emitter that ionizes the xenon gas injected at the front of the discharge source canister. The canister itself is lined with appropriately placed magnets designed to contain the plasma within the source and limit the flow of electrons and ions to the walls. A negatively charged grid is mounted at the back of the discharge chamber, to which an electrically isolated ceramic

sample wall can be mounted. An electrical schematic of the plasma source operation is shown below in Figure 4.

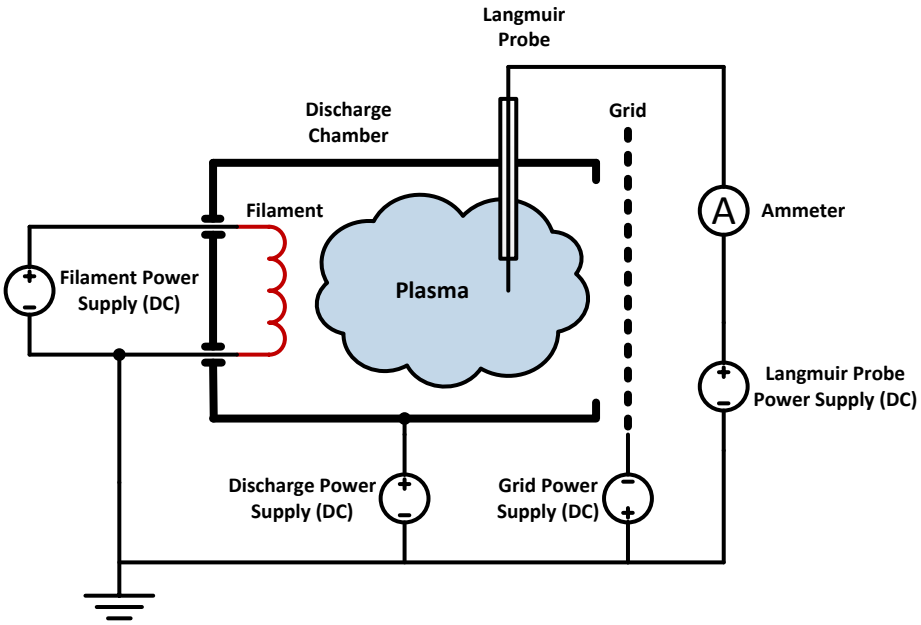

Figure 4 Schematic of plasma source operation with langmuir probe circuit.

The ceramic sample is mounted such that its edge is visible through the window on the side of the canister through which the LIF signal is collected. Figure 5 shows a model of the plasma discharge source, with the interrogating laser beam and fluorescence signal orientations shown. The input beam is directed into the discharge source normal to the ceramic wall face through a small hole and is blocked by the ceramic wall. The incident light is therefore parallel to the direction of the xenon ion acceleration allowing for observation of the Doppler shifts in the LIF signal.

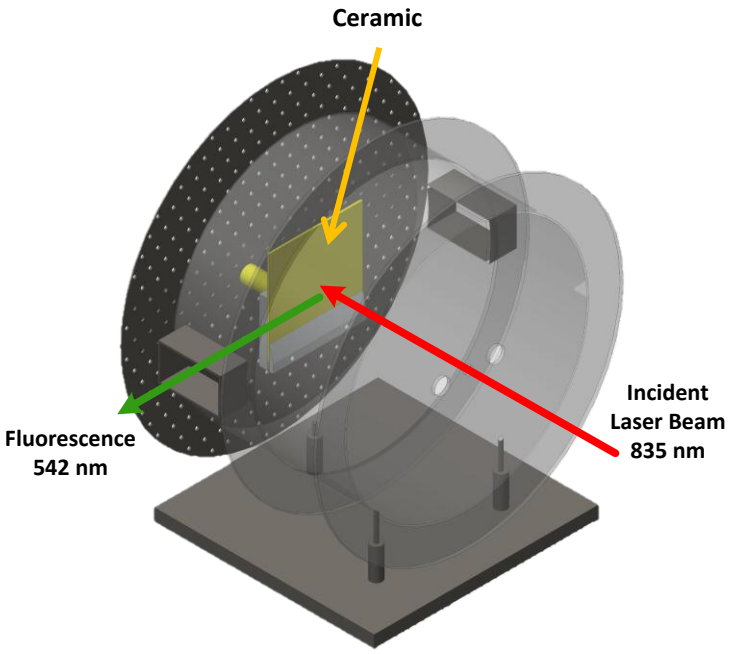

Figure 5 Schematic of plasma discharge source.

The plasma discharge source also features access holes on the top of the canister through which Langmuir probes can be inserted into the plasma. The Langmuir probes provide a means of determining the plasma conditions, such as electron density, ion density, electron temperature, and bulk plasma potential during operation of the plasma source.

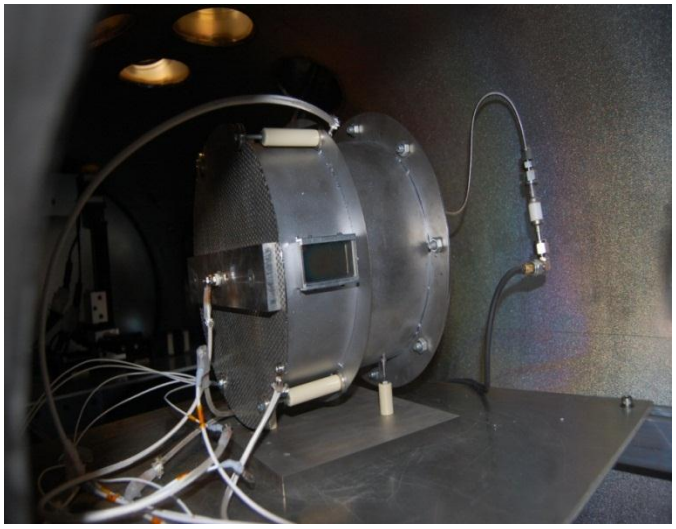

Figure 6 Photograph of Plasma Source installed in University of Michigan's PEPL facility.

The plasma source was installed into a vacuum chamber (Ø35 cm, 1.2 m long) in Colorado State University's Laser and Plasma Diagnostics Laboratory (LPDL). The chamber is fitted with a turbomolecular pump (Leybold-Heraeus turbovac 150) and roughing pump combination which is capable of achieving a base pressure of ~5 µtorr. The chamber is also fitted with a mass flow controller (MFC, Unit 7360) for accurate control of xenon gas flow from 1-50 sccm.

In order to facilitate fine spatial resolution in the LIF measurements for which this plasma source was created, the primary design criteria required that the source was capable of creating low-density plasmas with thick plasma sheaths (~1 cm). Initial characterization of the plasma source showed successful creation of plasmas within the desired plasma density range using argon and documentation of these tests were provided to CSU upon delivery. The LIF experiment, however, was intended to be conducted with xenon so further characterization was required to ensure that xenon operation resulted in similar plasma conditions under the same power supply and xenon flow conditions.

Langmuir probe measurements, however, revealed drastic inconsistencies between the documented argon plasma densities and those measured during xenon plasma operation. When operating the plasma source for day to day work optimizing the LIF procedure, the plasma source was always run at power supply and mass flow controller settings listed in the documentation. As an example, one such test called for a filament current of 8 A, discharge voltage of 30 V and a Grid voltage of -15 V. These values were held constant while the filament voltage and current of the discharge chamber and grid were measured at those previously described settings. Langmuir probe data gathered at these conditions are shown in Figure 7 and Figure 8.

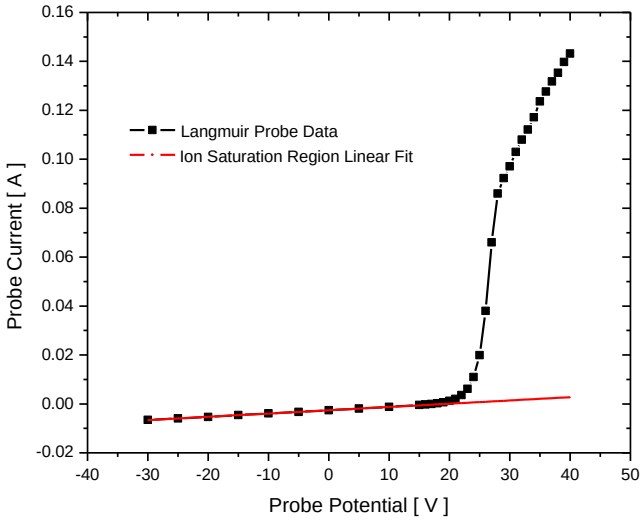

Figure 7 Langmuir Probe data with Linear fit of Ion saturation region for extrapolation to ion saturation current at plasma potential.

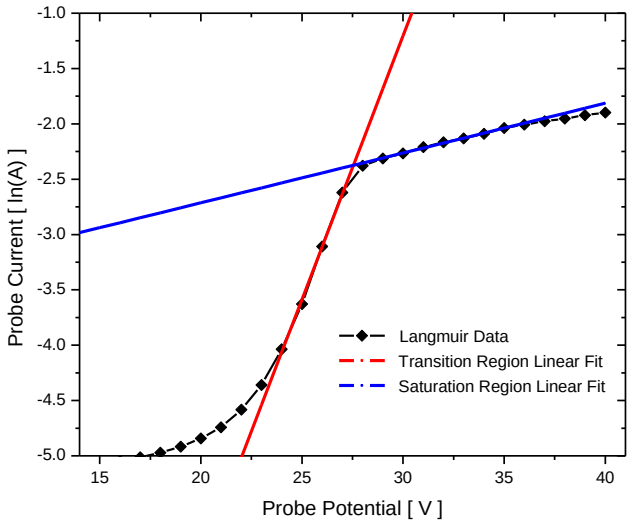

Figure 8 Natural Log of Langmuir probe data with linear fit lines of transition and electron saturation regions for determination of electron saturation current and plasma potential.

This specific test was run with 7 sccm of xenon flowed into the discharge chamber and had a measured electron temperature of 2.1 eV and ion density of $3.09 \cdot 10^{-12}$ cm^{-3}. The argon ion density provided in the documentation at these power supply and mass flow conditions, however, was reported to be $1.45 \cdot 10^{-10}$ cm^{-3} with an electron temperature of 3.4 eV.

The ion and electron densities found during the xenon operation tests at Colorado State University were typically 2-3 orders of magnitude above those measured by University of Michigan during their initial argon characterization. The higher density is advantageous when considering signal strength, as the fluorescence signal increases with increasing ion number density within the collection volume, but as can be seen in equation (1) higher density typically results in thinner sheaths. The resolution of the spatial measurements therefore would need to be much finer to resolve the structure of the sheath potential since changes occur over a much smaller distance. Achieving smaller spatial resolution can be easily achieved using optical

arrangements that allow for magnification imaging, however creating finer spatial resolution also reduces the fluorescence collection volume and therefore reduces the available signal for measurement. This unfortunate interplay between signal strength and spatial resolution led to a study of the signal and noise levels in order to determine any possible sources of noise that could potentially be mitigated or even eliminated to accommodate LIF measurements at lower plasma densities.

2.1.2 LIF EXPERIMENTAL SETUP

To excite the xenon ions into the upper energy state as described in section 2.1, a grating-stabilized laser diode (Toptica DL-100) is tuned to 835.954 nm to inject approximately 35 mW of laser power into the plasma. As shown in Figure 9, the laser beam is first directed through a Faraday isolator (Isowave I-7090C-L) to reduce unwanted fluctuation of the laser output caused by the back-reflection of light into the laser diode. Wavelength scanning of the external cavity diode laser is achieved through piezoelectric actuation of the laser grating using a feed-forward loop proportional to the laser current modulation. This arrangement allows for up to 22 GHz mode hop-free tuning range of the laser wavelength, which is a sufficiently large range to capture the velocity distribution profiles expected in this study (width of ~2 GHz). After the isolator, a small portion of the beam is picked off of the main beam using a beam splitter (~99:1) and directed into a frequency monitoring leg which includes an etalon (free spectral range of 2.31 GHz) and photodetector (Thorlabs PDA10CS) for determination of relative frequency. A detailed description of the frequency reference leg is provided in section 2.2.

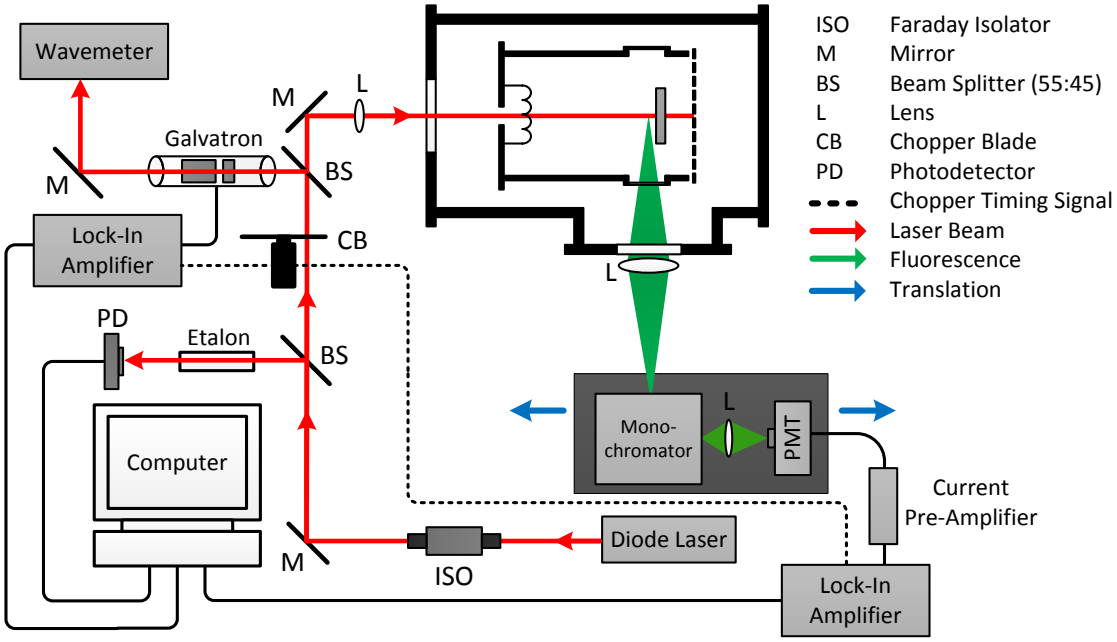

Figure 9 Schematic of experimental setup

Determination of the Doppler shifts also requires an absolute measure of the laser frequency axis; in particular the (zero-) frequency at which a stationary xenon ion absorbs light, for which an opto-galvanic cell (Hamamatsu L2783 Xe-Ne-Mo) is used. This cell, or galvatron, is a see-through hollow cathode lamp that creates a xenon-rich plasma between two cylindrical Mo tube electrodes through which a laser beam can be launched. The hollow cylindrical electrodes are housed inside a 25 mm diameter, 120 mm long glass cylinder with angled entrance and exit windows, designed to prevent retro reflection. The glass cylinder is filled with approximately 3 torr of neon and 4 torr of xenon filler gas with which the plasma is created. As the laser passes through the plasma, a fraction of the xenon ions (or neutrals) are excited by the incident photons, thereby altering the conductivity and inducing a measureable change in the plasma current. This current is detected through a ballast resistor circuit, shown in Figure 10,

which includes a high pass RC circuit as well as transient suppression to protect the lock-in amplifier (LIA) from high voltage spikes.

The transient suppressor circuit design is slightly different than conventional transient suppression circuits which typically two Zener diodes in series in opposite directions across the signal terminal to act as an open circuit when voltages are below the reverse breakdown voltage of the diode. In this arrangement, the two diodes act as a short when voltages exceed the breakdown voltage (in either bias direction), effectively rerouting the voltage spike back into the galvatron circuit instead of spiking across the signal terminal and potentially damaging equipment. The sensitive front-end electronics in the LIA used in this research required very low voltage transient suppression (above ~2 V). This low of reverse breakdown voltage is not typically found in Zener diodes because the voltage required to create a shorted diode in the forward direction is typically only 1.5 V. By placing the diodes (NTE135A) in parallel with each other, as shown in Figure 10, the forward bias voltage can be used as the transient suppression limit since below that 1.5 V both diodes act as a circuit open.

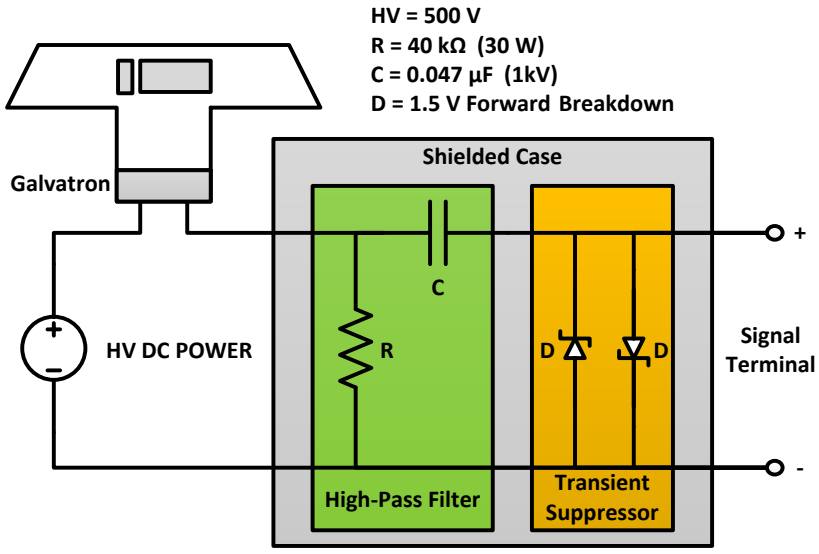

Figure 10 Laser Galvatron Circuit with high-pass RC circuit and transient suppression

The laser galvatron is operated at 500 V in order to achieve stable plasma conditions at the suggested 10 mA of operating current to the circuit. As the laser is scanned across the Xe transition wavelength, the dip in current can be used to locate the absolute transition wavelength. Approximately 18 mW of the main laser beam is split away and directed through the galvatron, leaving approximately 35 mW of laser power in the main beam (after various optical losses) to be directed into the plasma source for LIF procedures.

The main beam is directed into the vacuum chamber through a window (5.1 cm diameter) formed of N-BK7 glass with anti-reflection coating (650-1050 nm). The beam is then directed through the center of the plasma source at the dielectric sample wall. Another window (5.1 cm diameter) N-BK7 window with anti-reflection coating (350-700 nm) allows for the LIF light to be collected by optics outside of the chamber at a collection angle of 90˚ from the laser path. The fluorescence is imaged (1:1) using a 150 mm focal length lens onto the 120 μm entrance slit of a monochromator (EG&G PARC 1229) set to transmit light at 542 ±1 nm in order to filter optical interference from the broadband tungsten filament emission. The imaging of the fluorescence onto the plane of the entrance slit (120 μm) allows for collection from a finite detection volume along the beam path, and defines the minimum spatial resolution of the LIF measurements based on the slit width that is used. These aspects will be further discussed in section 4.1.

Light exiting the monochromator is finally detected with a photomultiplier tube (PMT, Hamamatsu R3896). A short focal length lens is used to focus, the exiting light onto the small effective area of the PMT face. The PMT signal is amplified using a variable gain current preamplifier (Oriel 70710) at 10^8 V/A to convert the current signal to a voltage signal for ease of detection. To increase the signal-to-noise ratio (SNR) of the fluorescence signal as well as the galvatron signal, a chopper wheel (Thorlabs MC200) is used in conjunction with two separate

dual phase lock-in amplifiers (LIA, EG&G 5210, SR810). Optimization of the LIA operation will be described in section 2.2.

As shown schematically in Figure 9, the lens used to image the LIF fluorescence onto the monochromator face remains fixed with respect to the plasma source and incoming infrared laser beam. The monochromator and PMT, however, are mounted on a platform such that they can be translated as a unit along the beam axis using a translation stage mounted to the bottom of the platform. By translating the monochromator, stage the collection volume from which the fluorescence signal is gathered can be spatially scanned along the beam line. The translation stage micrometer allows for accurate translation with 25 μm resolution.

2.1.3 DATA PROCESSING PROCEDURE FOR DOPPLER SHIFT MEASUREMENTS

Data collection employed a 4-channel oscilloscope (Tektronix TDS 5034B) for simultaneous acquisition of LIF, galvatron, etalon and laser scan timing signals for subsequent data processing using a customized Matlab code. A sample of the unprocessed data is shown in Figure 11.

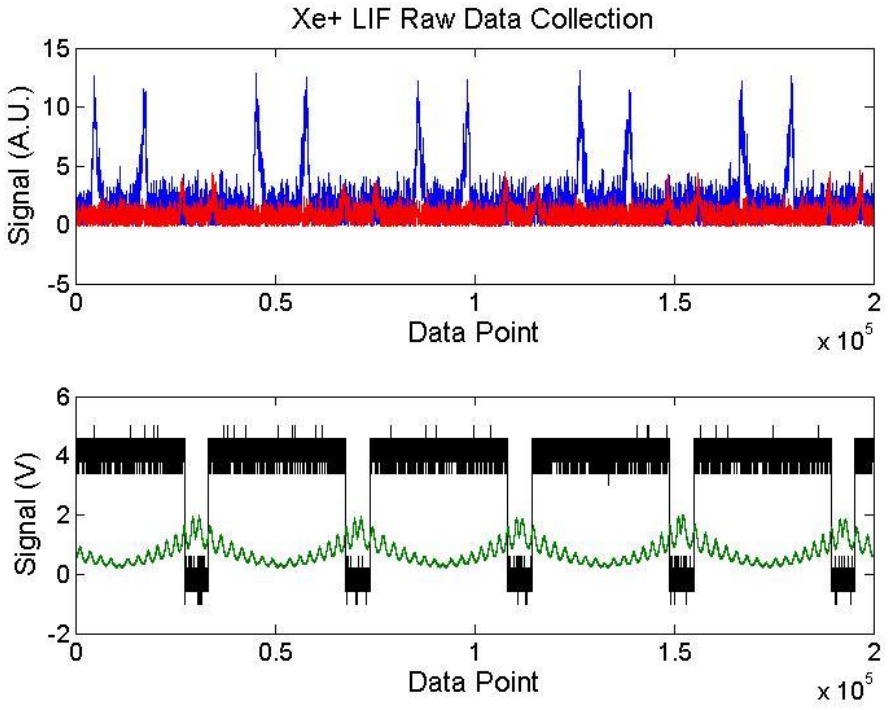

Figure 11 Raw data gathered for Doppler shift measurements. Top: LIF Signal (blue) and Galvatron Signal (red). Bottom: Laser Scan Timing signal (black) and Etalon Signal (green).

In a given test, data was gathered over many consecutive laser scans. This data was sampled at a rate which varied from test to test depending on the number of scans desired for a certain data set. The data must therefore be split into individual frequency scans using the timing signal (black) so that each LIF and galvatron pair from a single up or down ramp of the laser frequency can be analyzed separately for Doppler shift measurements. The timing signal is a square-wave output of the laser controller that places the frequency scan's "turn-around" peak in the center of a short 0 V valley. Using the symmetry of the triangle wave between these valleys, the LIF, galvatron, and etalon data are cut into individual traces and separated into those during frequency "up-ramps" and those during "down-ramps". These traces must be separated into up and down-ramps due to a noticeable hysteresis of the laser scan, which necessitates separate

calibration to ensure accuracy of the frequency axis. Frequency axis calibration is achieved through two steps: relative frequency spacing determination using the etalon signal and absolute frequency calibration from the galvatron signal.

The etalon signal is analyzed first to stretch the frequency axis of the gathered data to account for the hysteresis and non-linearity of the laser wavelength scan. This is achieved by locating the position of each etalon peak within the scan. The spacing between two peaks is known to be exactly one FSR of the etalon (2.31 GHz), so each peak is paired with an FSR value (starting with 0 then proceeding to 2.3073, 4.6146, etc.). FSR value is then plotted against the peak position, shown in Figure 12, and the resulting line is fitted using a 2nd order polynomial.

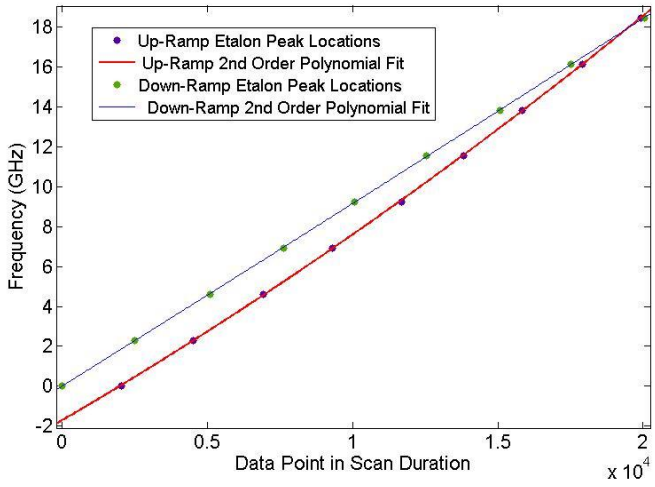

Figure 12 2nd order polynomial fits of etalon peak locations for frequency calibration of laser scan.

These equations provide a means to calculate the spacing of the frequency axis which, until this stage, is merely an indexed data point within a scan trace. Using the first data point within one of these scan traces as a 0 GHz starting point, the LIF and Galvatron signals can then be plotted against relative frequency as shown in Figure 13.

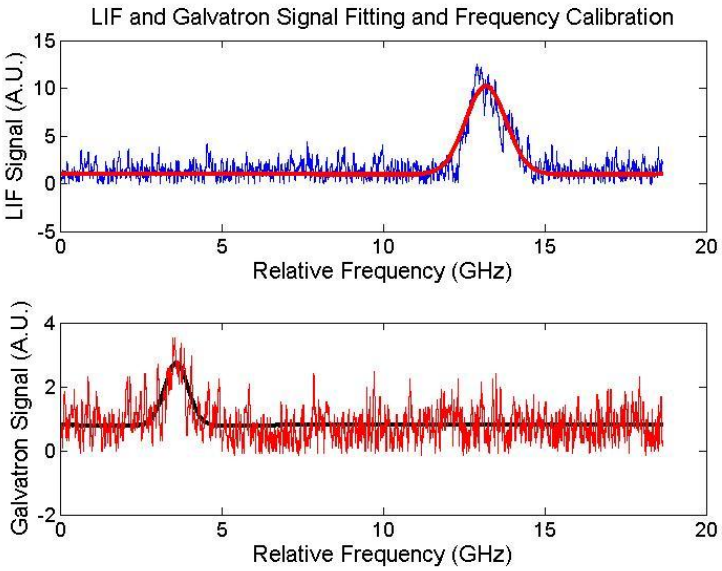

Figure 13 LIF (top, blue) and Galvatron (bottom, red) signal fitting and frequency calibration.

The LIF and galvatron signals are fitted using simple Gaussian lineshape functions which provide transition feature centers. As discussed in section 2.1.2, the center frequency from the galvatron is a known frequency corresponding to the neutral xenon transition at 834.975 nm. Using the galvatron center from the Gaussian fit and that transition's known spacing from the xenon ion transition at 834.954 nm, a fully calibrated frequency axis of the LIF data is finally set. A sample plot of an LIF trace with calibrated frequency axis (0 GHZ relative frequency corresponding to 834.954 nm Xe+ absorption transition) is shown in Figure 14. This frequency can be easily converted to velocity by multiplying these frequencies by the transition center wavelength of 834.954 nm.

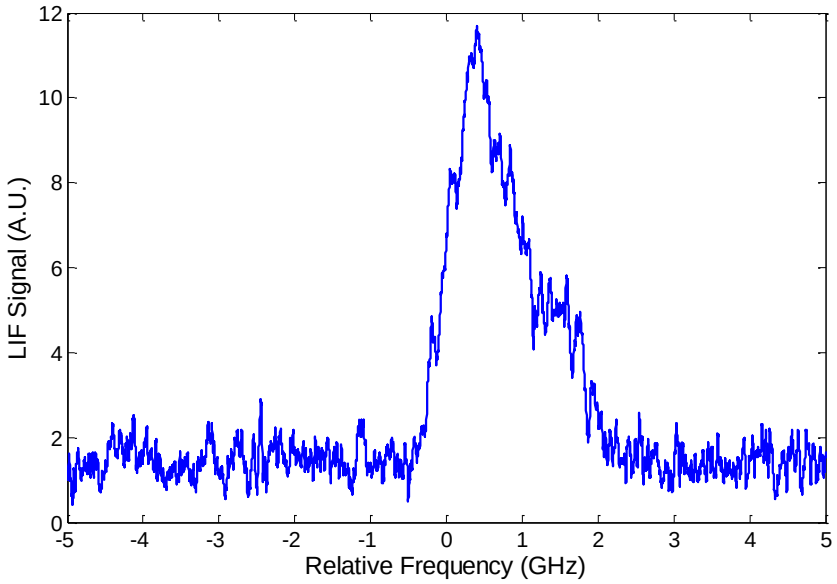

Figure 14 LIF signal trace with calibrated frequency axis. 0 GHz corresponds to Xe+ absorption line center at 834.954 nm.

2.2 OPTIMIZATION OF THE LIF VDF MEASUREMENT PROCEDURE

During the development of the LIF IVDF measurement technique discussed in this thesis several studies of various aspects of the apparatus and procedure were conducted to improve the detection limit and accuracy of the system. This section will discuss the IVDF measurement procedure developed in these studies.

2.2.1 OPTO-GALVANIC CELL

The optogalvanic cell, as described in section 2.1.2, is a hollow cathode lamp containing a plasma through which one can direct a laser beam to gain spectroscopic information. The cell

used in this study was chosen specifically with Xenon and Neon as the filler gases in order to utilize the same xenon ion absorption line used in the LIF measurements. The same galvatron model was used by Huang et al. [21] for stationary wavelength reference. By using the same xenon ion transition used in the LIF measurements, the absorption feature can locate the transition wavelength for an unshifted absorption spectrum, which can then be used to calibrate the frequency (wavelength) axis for the Doppler shifted measurements.

Initial testing of the xenon absorption line at 834.954 nm (vacuum) using the galvatron, however, proved to be very difficult. It was only possible to detect the absorption line by using the entire 75 mW of beam power with significant filtering by using the LIA at long time constants (τ =10 s). It was discovered through experimentation with the galvatron that neutral xenon transitions can also contribute an opto-galvanic signal. A nearby neutral xenon transition at 834.975 nm was therefore used instead of the 834.954 nm transition as an absolute wavelength reference due to its larger opto-galvanic signal which is detectable with approximately 10 mW of laser power.

2.2.2 LOCK-IN AMPLIFIER

Using the neutral xenon transition to calibrate the frequency axis requires a relatively large scan extent (~ 18 GHz) to detect both the LIF and galvatron signal in the same laser scan. The Toptica DL100 laser used in this research provides sufficient mode-hop free tuning of the laser wavelength to accommodate this scan range, but laser controller settings only allow for a minimum scan frequency of 5 mHz (period = 200 sec). These limits define a minimum scan speed of ~90 MHz/s and therefore set a necessary maximum time response based on the width

and amplitude of the LIF signal as the laser scans across the transition. The time response of the collection system is limited by the LIA time constant, which leads to a trade-off against noise filtering and SNR.

The SNR of the LIF measurement is critical to the accuracy of the Gaussian fit that determines the transition frequency center (and sheath potential change). Inappropriate choice of LIA time constant can artificially stretch and shift the absorption feature by creating a time delay between the real-time etalon frequency monitoring and the LIA output signal. A simple study was performed at 90 MHz/s to determine the maximum time constant allowable without distorting the LIF feature. Figure 15 shows the results of that test, with traces corresponding to LIA time constants (tau) between 30 ms and 3 s.

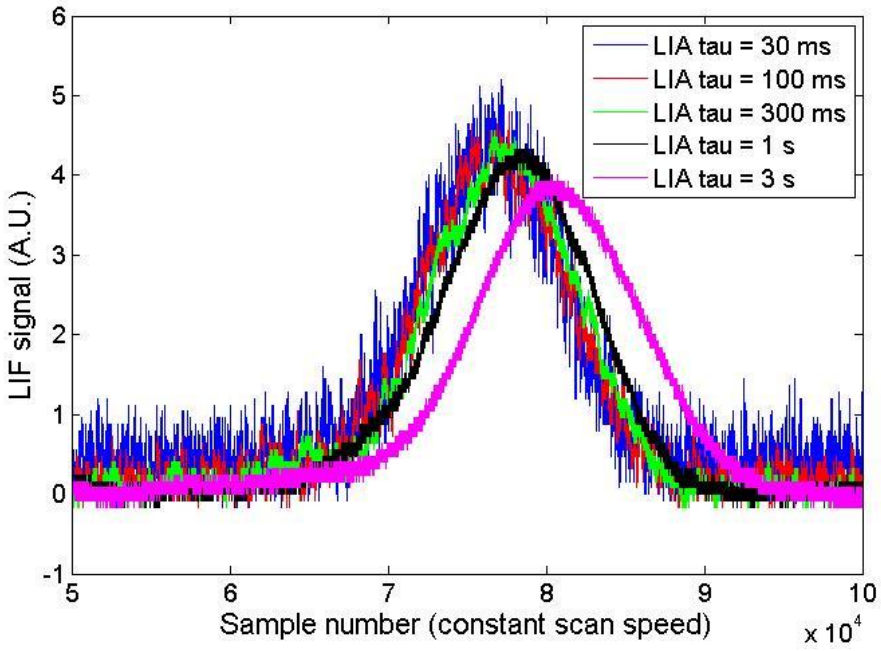

Figure 15 Lock-In Amplifier Time Constant response study, large scan range

The LIA amplifier was first operated at the smallest time constant setting of 1 ms and increased after each complete scan, but the data shown does not include traces between 1 ms and 10 ms because they did not exhibit any distortion. The shorter time constant settings (30 ms and 100 ms) show decreased SNR, but no distortion while time constants of 300 ms and higher show clear distortion. The LIA amplifier was therefore operated with a 100 ms time constant, allowing for maximum noise filtering without artificial distortion of the LIF spectral measurements.

2.3 OPTICAL NOISE STUDY

The goals of the optical noise study were to determine the sources of optical and/or electrical noise in the collection system, quantify those noise contributions and ultimately determine the plasma density LIF detection limit. The detection limit of the system was determined from the signal to noise ratio (mean divided by standard deviation) of the LIF signal at peak fluorescence. All noise study measurements were conducted under typical operational plasma conditions: filament current of 8 A (26 V), discharge current of 1.99 A (25.84 V) and grid voltage of -15 V (154 mA). Prior to operation, the vacuum chamber was pumped down to 5 μtorr, then during operation the plasma source was supplied a xenon flow rate of 1 sccm resulting in a chamber pressure of ~70 μtorr. Figure 16 shows a single LIF scan measured with a LIA time constant of 100 ms and 30 mV sensitivity setting, PMT voltage of 550 V, and pre-amplifier gain of 10^8 V/A. The laser scan range was set to 16 GHz centered at 835.963 nm and a scan period of 200 s (5 mHz). This scan resulted in a peak average of 10.7 V, a (baseline) standard deviation of 1.2 V and therefore a SNR of 9.1.

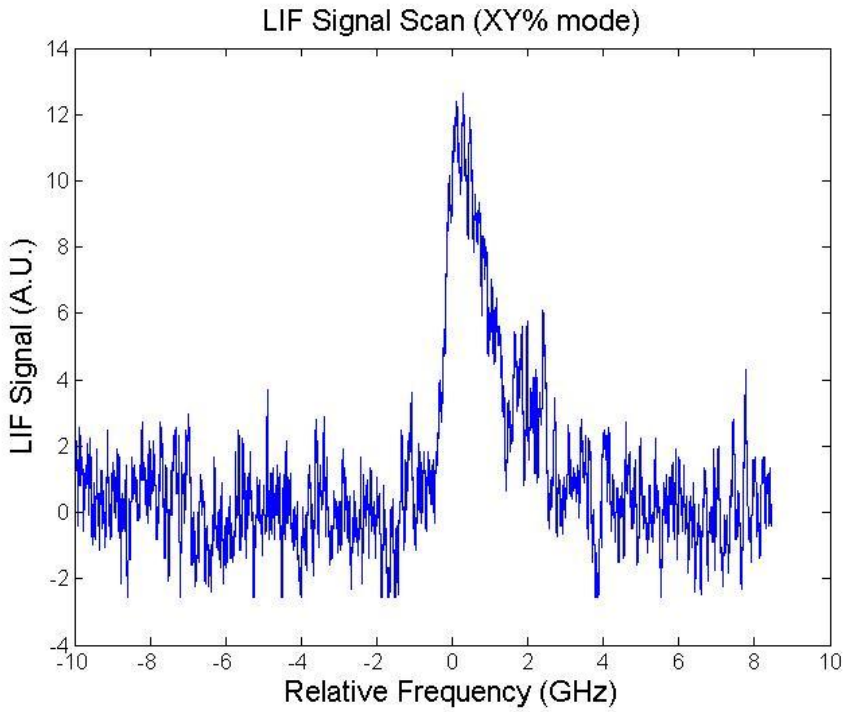

Figure 16 Raw LIF data from single frequency scan (~3.5 min) SNR = 9.1. Relative frequency axis centered (0 GHz) at 834.954 nm Xe+ absorption transition wavelength.

For additional characterization, a spectrometer (Ocean Optics HR4000) was used to gather a broad spectrum of the light emitted from the plasma and filament during normal operation. Figure 17 shows the light spectrum collected directly out of the vacuum chamber LIF collection window before entering the monochromator. Spectra were measured with the plasma and filament on, as well as with filament only (by turning off the flow to the anode). The spectrum shows plasma luminosity at the 542 nm collection wavelength that is similar in brightness to the filament, though it appears weaker due to low-resolution of the spectrometer grating.

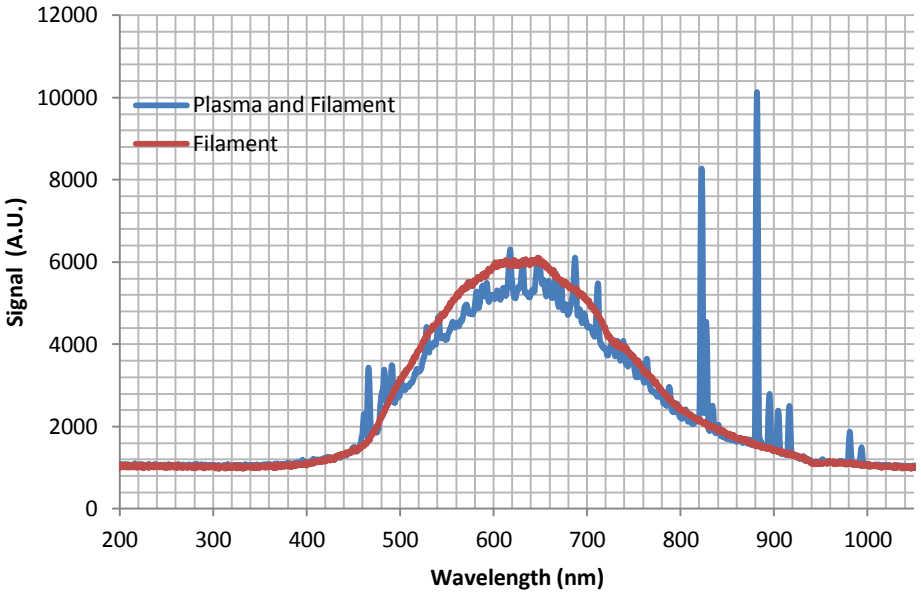

Figure 17 Plasma and filament spectra during operation

The next test conducted in the optical noise study was to quantify the effect of the luminosity seen in Figure 17. The test looked at the noise contribution from the plasma with the interrogating laser turned off. Figure 18 shows the LIA output during normal operation of the plasma source (left) and operation without the plasma with only filament noise (right). With both the plasma and the filament contributing to the optical noise, the LIA output noise showed a standard deviation of ~1.1 V while the contribution from the filament only was ~0.8 V. The overall LIF noise (SD =1.2 V), as shown in Figure 16, is clearly dominated by the light from the filament and the plasma (SD = 1.1 V). Assuming that these noise sources add in quadrature, this implies that ~50% of the noise is coming from the filament luminosity and ~50% comes from the plasma luminosity itself.

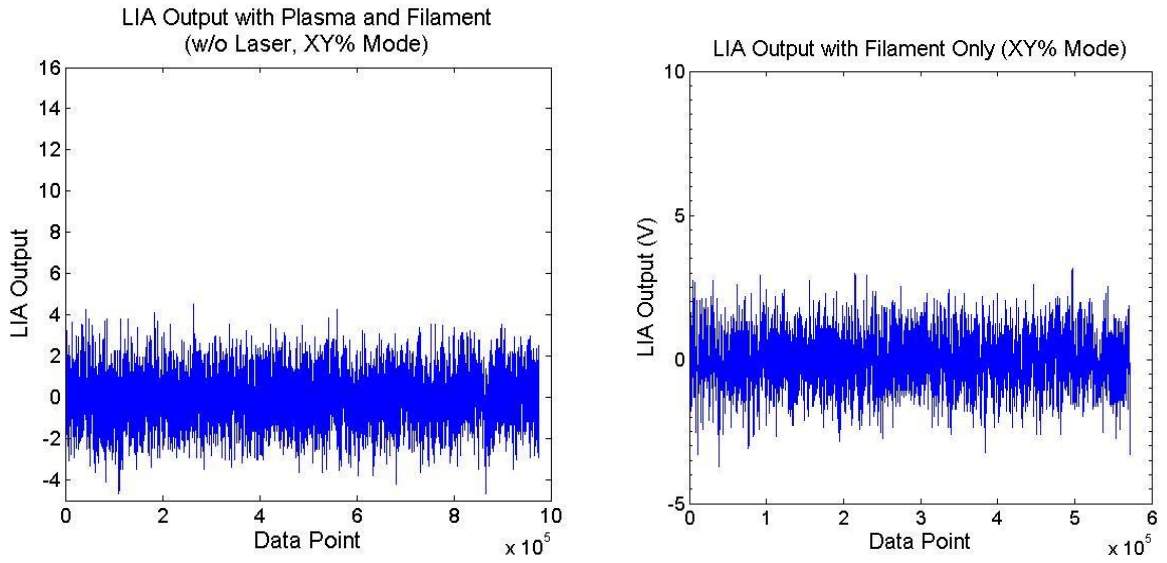

Figure 18 Optical noise contributions of plasma and filament SD = 1.14 V (left) and filament only SD = 0.85 V (right).

The following test sought to quantify the LIA and preamplifier noise contributions in absence of the plasma or filament luminosity. Obviously, it is not possible to obtain an LIF signal without the filament and plasma. An "artificial LIF signal" was therefore created to recreate the same collected light level as that measured in the LIF trace shown in Figure 16. A green Helium-Neon laser (He:Ne) emitting at 543.5 nm was overlapped with the interrogating infrared beam, using a flip mirror between the Faraday isolator and the first steering mirror and passed through the optical chopper. The beam follows the same path as the infrared beam and is blocked by ceramic sample at the rear of the discharge source where the green light is scattered off of the surface. The He:Ne wavelength is close enough to the xenon fluorescence wavelength that adjustment of the monochromator grating position is not necessary to still detect a signal in the monochromator output. By adjusting the He:Ne power using neutral density filters, the power of the scattered light was precisely matched to that of the LIF signal. The data shown in Figure 19 were gathered using this technique and have a standard deviation of only 0.21 V. This

shows that, for the given LIF signal power, the LIA and preamplifier settings allow for a SNR of 48 in absence of plasma and filament luminosity.

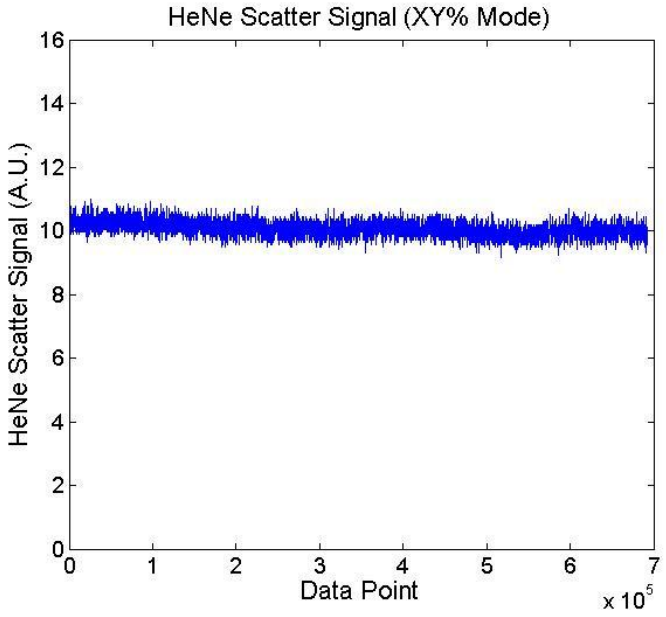

Figure 19 He:Ne scatter equivalent LIA signal. No LIF, plasma or filament; elastic scatter of He:Ne laser (543.5 nm) SNR = 48

We also examined raw luminosity and He:Ne scatter directly out of the PMT without LIA filtering. In these tests, the PMT signal was directly connected to an oscilloscope (1 MΩ input impedance). Raw PMT data of the artificial LIF signal (He:Ne scatter) was also gathered and is plotted in Figure 20 with the raw PMT luminosity data corresponding to the plasma operating conditions from the initial optical noise study (Figure 16). The plasma and filament luminosity in Figure 20 is ~30 times larger than the LIF signal at the plasma conditions used in this noise study.

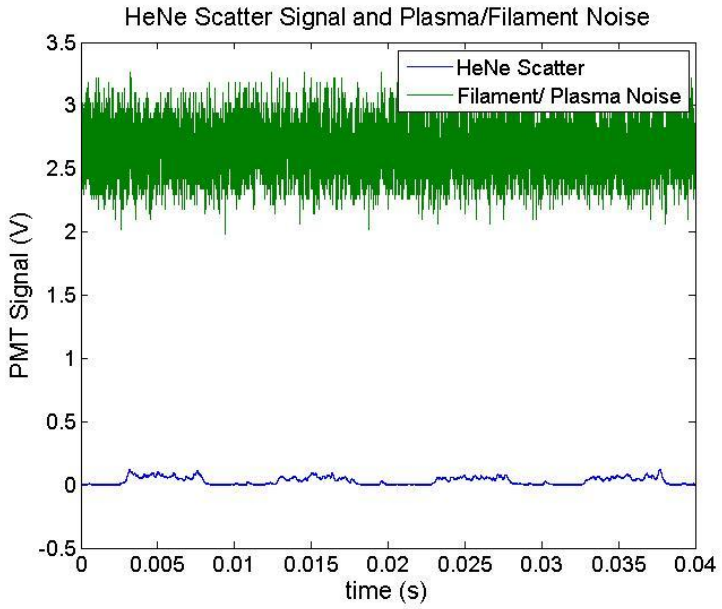

Figure 20 He:Ne Scatter Signal (raw PMT) and Plasma/Filament Noise

The final experiment in this optical noise study sought to quantify the SNR improvement achievable with averaging and, using this information, extrapolate the decrease in noise to determine a minimum plasma density at which a reasonable SNR can still be achieved. Under the same plasma and optical collection settings used throughout this study, 25 LIF signal traces were recorded at the same spatial position. Then, using the Matlab code described earlier, the LIF signal was averaged over 5, 10 and 25 traces and analyzed to determine the resulting SNR. As shown in Figure 21, the SNR improves at approximately the square root of the number of traces averaged; after 25 averages the SNR improved from 14 (first trace) to 70.

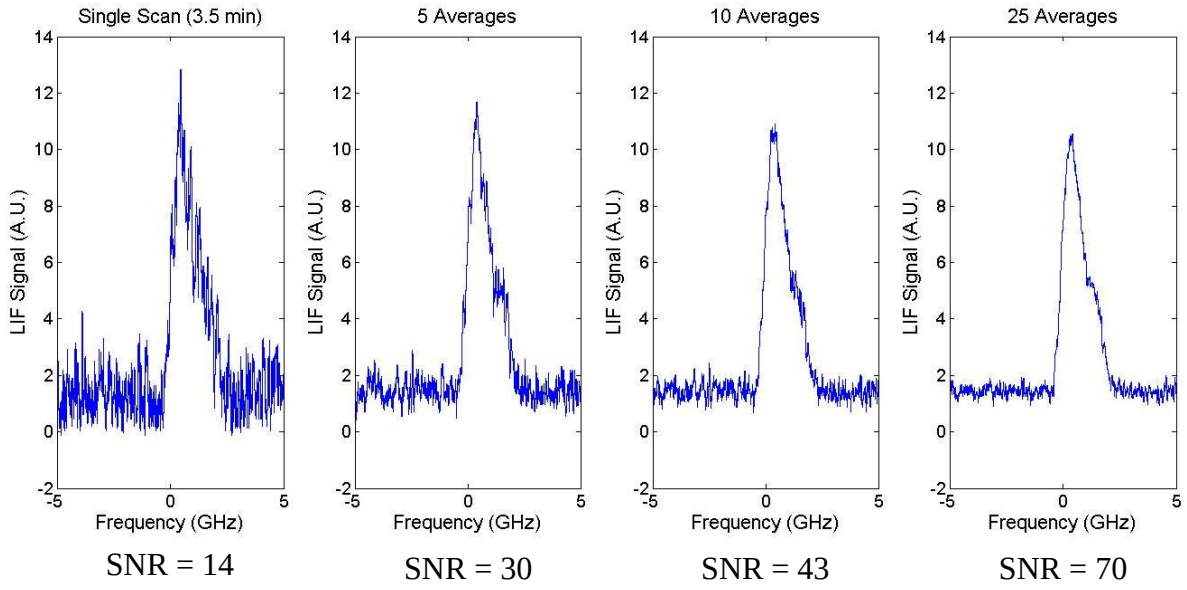

Figure 21 Xenon LIF Signal Traces with Averaging to improve SNR

This amount of averaging, however, requires ~90 minutes to gather. Assuming proportional scaling of the fluorescence signal strength with plasma density, averaging 25 signal traces would allow for a SNR of 10 at a plasma density of $n_i = 1 \cdot 10^{11}$ cm^{-3}. This amount of time presents some difficulties in the form of possible mechanical drift of the collection optics as well as stability of the plasma density during long term operation, but should be possible.

In order to reduce this detection limit to much smaller plasma densities, the luminosity of the plasma and filament must be reduced significantly. The signal strength of the collected fluorescence is fundamentally limited by the plasma density and therefore cannot be increased to improve the system's SNR. With the current limiting factors of scan speed and LIA time constant, reduction of noise levels must occur in order to improve the SNR enough to facilitate plasma sheath measurements. For these LIF sheath measurements to ever be possible either a reasonable SNR must be attainable at lower plasma densities to stretch the sheath thickness to

accommodate the current spatial resolution or the spatial resolution must become fine enough to resolve the potential changes in the thin sheaths at the current plasma conditions. Currently the spatial resolution of the system is defined by the monochromator entrance slit width (120 µm) on which the unmagnified fluorescence is imaged. Increasing from 1:1 to 4:1 imaging (4x magnification) would therefore reduce the spatial resolution of the measurement to a 30 µm segment of the interrogating beam path. The monochromator and PMT stage is also mounted on a micrometer actuated translation stage with ~25 µm resolution.

According to work done by Lee et al. [8] Doppler shifting within the sheath is evident out to 3-10 Debye lengths from a surface, so if roughly 10 local potential measurements are desired within the plasma sheath, the spatial resolution must be on less than or equal to the Debye length. The SNR of the current configuration sets a minimum ion density of $\sim 5 \cdot 10^{11}$ cm^{-3} at which the LIF signal strength is still detectable with reasonable SNR of 10. At these conditions the Debye length is still roughly 60 µm which only allows for only 5 points within the sheath with the current 120 µm spatial resolution. As mentioned earlier, either the spatial resolution fo the LIF measurements must be made finer or the SNR ratio must be increased to allow for lower density plasmas (and thus thicker sheaths) to be measured. Section 4.1 will discuss the possible methods for improving the LIF system to achieve one of these two options.

2.4 PRELIMINARY MEASUREMENT OF DOPPLER SHIFTED IVDFS IN PLASMA SHEATH

Despite the poor SNR and rough spatial resolution of the current system, preliminary tests were conducted in an attempt to detect possible Doppler shifting in the considerably thicker

presheath region. Figure 22 shows data gathered at 1.27 mm (0.05") increments from the ceramic wall.

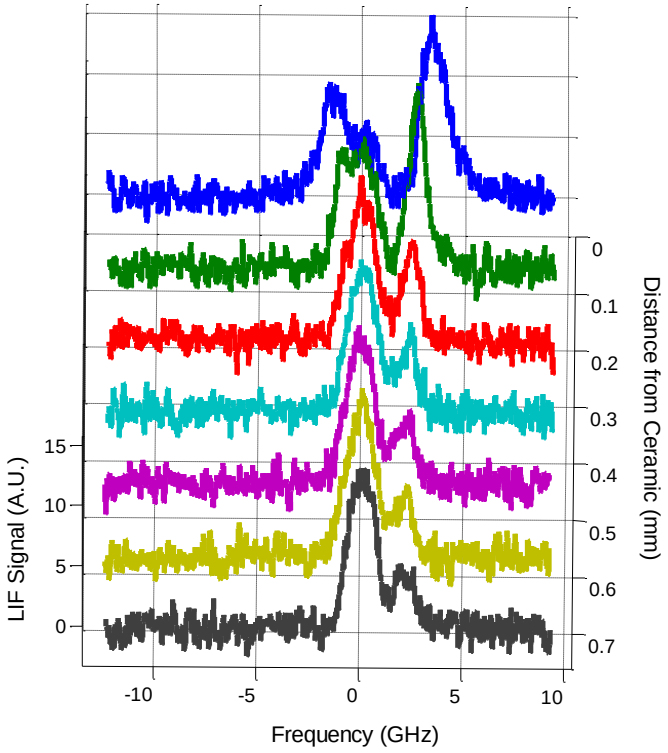

Figure 22 Preliminary spatially resolved Xe+ LIF IVDF with evident shifting.

The data shown in Figure 22 clearly shows multiple features around the 834.954 nm Xe+ transition. The feature on the right (higher frequency) shows clear shifting of the feature's center frequency towards even higher frequencies as the measurement position moves closer to the wall. This is the expected trend for xenon ions accelerating towards the negatively biased wall in the same direction as the incoming laser beam. The other feature, however, is not consistent with the expected blue-shifting of the Xe+ absorption transition and therefore presents another issue with the current LIF configuration that must be addressed. It is hypothesized, though not proven, that the extra feature results from laser light reflecting off of the ceramic surface and is then absorbed by the xenon ions at red-shifted frequencies since the reflected light is now

travelling in the opposite direction of the ion acceleration toward the wall. If this theory is correct, this problem could be solved by introducing a small hole in the ceramic sample through which the beam can pass to prevent reflection of the interrogating light source. This, and other improvements mentioned in this chapter, will be discussed in more detail in section 4.1.

2.5 SHEATH POTENTIAL CALCULATION AND ERROR PROPAGATION

Despite the lack of clear, spatially resolved changes in Doppler shifting within the IVDF data recorded thusfar, it is still useful to understand the sheath potential calculation process and the error associated with the current procedure. As discussed in section 2.1, equation (4) is used to determine the local potential using the IVDF center calculated using the Gaussian fit of the LIF data (shown in Figure 13). The error related with this sheath potential calculation, therefore, begins with the goodness of the Gaussian fit and the accuracy with which and IVDF center can be determined. Using conventional error propagation techniques with one source of error, the uncertainty in a given potential measurement is given by:

$$\sigma_\phi = \left[\frac{\partial \phi}{\partial \nu}^2 \ {\sigma_\nu}^2\right]^{1/2} \tag{5}$$

Which simplifies to:

$$\sigma_\phi = \frac{m_i {\lambda_0}^2}{e}(\Delta\nu)(\sigma_\nu) \tag{6}$$

where σ_ϕ is the uncertainty in the sheath potential calculation, $\Delta\nu$ is the Doppler shift in frequency of the IVDF center, and σ_ν is the uncertainty associated with the IVDF center measurement determined by the 95% confidence interval of the Gaussian fit. A representative data set was chosen which showed a Doppler shifting of 0.455 ± 0.003 GHz (relative to the stationary ion absorption frequency) and when used with the above equations resulted in a potential of -1.9 ± 0.0014 V. Using this uncertainty as a representative value of minimum measurable potential change and assuming this change would be measured over one increment of spatial resolution (120 μm), the minimum measurable electric field based on the current level of uncertainty in the procedure is 0.112 kV/cm. Using a coarser spatial resolution would provide smaller uncertainty in the electric field but at the expense of capturing less points within a given sheath.

3. CAVITY ENHANCED POLARIMETRY FOR ELECTRIC FIELD MEASUREMENTS IN GASES

Electric field measurements based on the Kerr effect, which takes advantage of the electric-field induced linear birefringence (i.e. different indexes of refraction for different linear polarizations), have been conducted in the past with some success. Early work has examined the Kerr effect in gases at high pressures (~10-100 bar) for which the induced birefringence is relatively strong [22], [23]. Often, a linear dependence of the Kerr constant on number density is assumed in order to extrapolate to lower pressures and estimate the birefringence at ambient conditions. More recent work, summarized below, has used sensitive optical techniques to study the Kerr effect at lower pressures including atmospheric pressure.

One recent experiment has directly measured the Kerr constant of air at ambient conditions, in a laser multi-pass configuration [24]. The path length used in that study was 13 m. Here, we describe a potentially more sensitive method, which may allow spatially-resolved measurements of moderate electric fields (~1-10 kV/cm) over small distances. We make use of the enhanced cavity length provided by a high-finesse optical cavity to accumulate the Kerr induced phase rotation over longer path lengths. Similar to cavity ring-down spectroscopy (CRDS), we exploit the large effective path-length provided by the successive reflections of optical radiation inside an optical cavity comprised of two highly reflective mirrors. As will be further discussed below, for mirror reflectivity of R=0.9999, one has a cavity finesse of approximately 30,000 and a path length enhancement of approximately 20,000 (in fact higher values are obtained in the present experiment).

Several experiments have employed cavity enhanced spectroscopy for measurement of birefringent effects. Circular birefringence (different indexes for left- and right-handed circularly polarized light) and circular dichroism (different losses for left- and right-handed circularly polarized light) have been studied via cavity ring-down polarimetry (CRDP) [25], [26]. In order to accumulate the polarization rotations (chiral effects) in a linear cavity, each of the cavity mirrors is preceded by a quarter wave plate which allow for accumulation of the polarization effects, but also add loss to the cavity and lower the length enhancement. Engeln et al. have performed polarization dependent CRDS where the rate of absorption is measured and the polarization dependent loss is inferred [27]. Polarization dependent absorption spectra for oxygen molecules in the presence of magnetic fields were recorded. The same research group has also shown a cavity enhanced absorption spectroscopy (CEAS) configuration where time-integrated absorption signals, as opposed to ring-down signals, are measured [28].

While polarization rotation due to circular birefringence does not accumulate over multiple passes in a linear cavity, effects of linear birefringence do accumulate. At first inspection this may not be obvious, since a medium with linear birefringence is equivalent to a wave plate, and wave plates are nominally reciprocal elements [29]. However, the reciprocity applies for phase conjugate beams, and in a cavity configuration the beam that re-enters the waveplate has undergone a reflection off the cavity mirror which does not provide a phase-conjugate. This is true for both metal and dielectric cavity mirrors, and is also very analogous to laser Q-switch configurations where the double passage through a quarter wave plate Pockels cell, after reflection off of a cavity reflector, causes a net polarization rotation of half a period. Indeed, the cavity enhanced Kerr effect has been studied using linear cavities. Bielsa et al. studied the Kerr effect of molecular oxygen by locking a laser beam to a ring-cavity [30]. The

electric field was modulated and a homodyne technique was used to measure the Kerr induced phase change. The closest work to ours is that of Inbar et al., who also used a laser locked cavity to enhance the phase change and who made measurements of the Kerr effect for CO_2, N_2, and O_2 at atmospheric pressure [31]. A key difference in our configuration is that we do not use an actively locked cavity so that our system is less technically demanding and potentially more amenable to implementations, such as for probing harsh discharge plasmas, where field strengths are comparable to those measured here and where cavity locking may be difficult. In past studies, electric fields in discharge plasmas have been made from measurements of emission [32] or from laser-induced fluorescence from excited states [33]. Finally, we mention that the Cotton-Mouton effect, i.e. magnetically induced linear birefringence, has also been studied with related cavity enhanced schemes [34], [35].

3.1 THEORY

Electric-field induced, linear birefringence is known as the Kerr effect. An applied static field affects the optical anisotropy of the medium through the difference, Δn, in the component of its refractive index along the direction parallel ($n_{\parallel}$) and perpendicular to the field ($n_{\perp}$):

$$\Delta n = n_{\parallel} - n_{\perp} \tag{7}$$

In electric birefringence, the optical Kerr constant [24], K, relates this difference to the static electric field strength, E:

$$\Delta n = \lambda K E^2 \tag{8}$$

where, λ is the wavelength, K is the wavelength-independent Kerr constant which is related to the wavelength-dependent Kerr constant, B, as $K = {B\lambda}/{n}$, where n is the index-of-refraction at λ (taken to be unity in this work as we are far from resonant transitions). In some cases, Kerr constants are expressed per unit number density, but more commonly the constants are reported for atmospheric pressure (with a linear scaling for number density)[36]. Numeric values of the Kerr constants for several gases are provided in Section 3.3. The phase shift induced between light polarized parallel and perpendicular to the static field, after traversing a distance L across the uniform field, is given as:

$$\theta_K = \frac{2\pi \Delta n L}{\lambda} \tag{9}$$

For ambient gases (e.g. N_2 and CO_2) in static fields of $E \sim 10^6$ V/m (=10 kV/cm), and over path lengths ~10 cm, the phase difference is on the order of micro-radians. The most straightforward measurement technique is to align the incident light at 45 degrees relative to the parallel and perpendicular field directions, and then to measure the light intensity through a nulled analyzer polarizer:

$$\frac{I_0}{I_i} = \sin^2\left(\frac{\theta_K}{2}\right) \tag{10}$$

where I_0 is the intensity transmitted through the nulled analyzer and I_i is the incident light intensity. For example, Kumada et al. have used this method but the smallest phase shift they

could measure was 50 micro-radians per pass [24]. The cavity enhanced method that we employ extends the effective path length, L_{eff}, thus providing larger phase shifts. Owing to the multiple passes within the cavity, the effective path length is found as:

$$L_{eff} = \frac{2FL_0}{\pi} \tag{11}$$

where L_0 is the actual cavity length, and F is the cavity finesse:

$$F = \frac{\pi\sqrt{R}}{1-R} \tag{12}$$

As a first approximation, the cavity enhanced signals that we measure can be analyzed using equations (9) and (10) but considering that the effective length is enhanced by a factor of $2F/\pi$ (from eqn (11)). For typical mirror reflectivity of R = 99.99% (finesse of ~30,000), the enhancement factor is significant, i.e. approximately 20,000. The resulting phase shifts accumulated over the multiple cavity passes are then in the milliradian range and more tractable for measurement.

In our experimental scheme, we scan the laser with a triangular current ramp such that it sequentially passes over multiple cavity resonances (i.e., cavity transmission peaks each separated by a free spectral range). As it crosses each resonance, light is coupled into the cavity and transmitted through the cavity. We measure, with crossed polarizers, the temporally integrated light due to each passage over a cavity resonance. The ratio of the crossed polarizer signals (parallel and perpendicular to the incident field) is dependent on the Kerr induced polarization rotation.

For fuller consideration of the behavior of light inside the cavity, and its birefringent effects, we perform an analysis of the temporal evolution of the optical signals and their polarization dependences. We use the infinite-sum approach of Morville et al. [37] to which we add birefringence. Equations (13) and (14) give the time-dependence of the electric field components parallel and perpendicular to the electric field directions:

$$E_{\parallel}(x,t) = \sqrt{T}E_{in}(x,t)\sum_{m=0}^{\infty} R^m \exp\left(i\frac{2\omega_0}{c/n_{\parallel}}\left\{\left[L_0 + v\left(t - \frac{x-L_0}{c/n_{\parallel}}\right)\right]m - \frac{v}{c/n_{\parallel}}L_0 m^2\right\}\right) \quad (13)$$

$$E_{\perp}(x,t) = \sqrt{T}E_{in}(x,t)\sum_{m=0}^{\infty} R^m \exp\left(i\frac{2\omega_0}{c/n_{\perp}}\left\{\left[L_0 + v\left(t - \frac{x-L_0}{c/n_{\perp}}\right)\right]m - \frac{v}{c/n_{\perp}}L_0 m^2\right\}\right) \quad (14)$$

Where $E_{\parallel}$ and $E_{\perp}$ are the parallel and perpendicular components respectively, T is the mirror transmission, x is position along the optical axis within the cavity, t is time, ω_0 is the laser frequency, L_0 is the cavity length, and v is the velocity of the moving cavity mirror (or the equivalent laser scan speed). In our model we take $n_{\perp} = 1$ and $n_{\parallel} = n_{\perp} + \Delta n$, where Δn is computed from equation (8) but with a multiplicative factor of L/L_0 to reflect the fact that the parallel plate electrodes do not fill the full cavity. The resultant electric field in a given direction, e.g. along the direction of the polarizer analyzer, can be found from the vector components and the intensity (as measured by a photo-detector) as the magnitude squared.

As an example of the polarization rotation, Figure 23 shows modeled signals due to passage through the optical cavity calculated using equation (10). The modeled case assumes a Kerr constant of B=10^{-18} m/V^2 (typical of gases [17]), electric field magnitude of E = 10 kV/cm

(giving Δn = 1.7x10^{-12}), input electric field polarizer polarized at 45 degrees to the parallel and perpendicular field axes, and cavity parameters of our current system as described below (cavity length of 90 cm, and R = 0.999982). The panel on the left shows the cavity output signal through an analyzer polarizer parallel to the input beam, while the panel on the right shows the cavity output signal through an orthogonal analyzer polarizer. The left panel is similar to a regular "ring-down trace" with a decay at roughly the $1/e$ time of the cavity, though in this case the laser is not extinguished by a modulator, rather the laser frequency is swept over the cavity resonance providing a natural extinction. The signal through the latter polarizer is due to the Kerr induced polarization rotation. Note that the vertical axis has a different scale and only a relatively small fraction of light passes through this polarizer. Because the phase of light in the cavity is continuously evolving, proportionally more light is transmitted through the nulled (orthogonal) polarizer at later time. Our measurement method is to measure the two signals shown in Figure 23 and to take the ratio of their areas, and then to use a model based on equations (13) and (14) to relate the area ratio to the applied field.

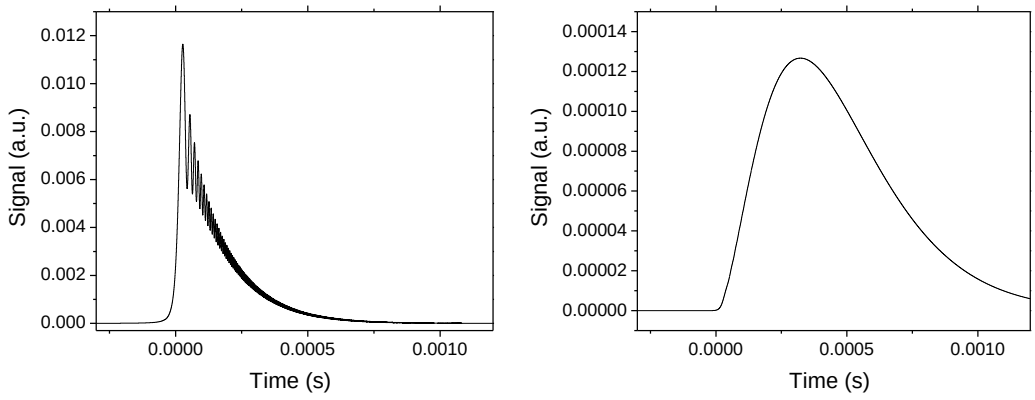

Figure 23 Left: Cavity output signal through an analyzer polarizer parallel to the input polarization. Right: Cavity output signal through an orthogonal analyzer polarizer.

As discussed below, our experimental scheme measures the light through both analyzer legs (parallel and perpendicular) as the laser is passed over a cavity resonance. We then ratio the areas of the two traces, e.g. for conditions of Figure 23, the area of the trace through the perpendicular polarizer to that of the parallel polarizer is 0.047. Although we use an analyzer polarizer and a trigger circuit with fast detector, the basic measurement is analogous to CEAS (also referred to as integrated cavity output spectroscopy). This measurement configuration is in contrast to CRDS where the light entering the cavity is extinguished (or a short pulse is used) and the subsequent ring-down decay is measured. Engeln et al. have derived expressions for polarization dependent CRDS based on ring-down time constants and loss rates [25] but these expressions do not apply to our experiment because they assume that light in the cavity does not begin to accumulate Kerr induced phase change until the start of the decay, as would be the case if a short pulsed laser were used, or the applied field were turned on with a switch at the start of the ring-down time. In our experiment, in contrast, the applied field is present continuously and the phase change begin to accumulate as soon as light enters the cavity and continues to accumulate during the full time that the light is in the cavity and the laser passes over a cavity resonance.

3.2 EXPERIMENTAL PROCEDURE

The cavity enhanced polarimeter is based on a continuous-wave (cw) CRDS setup at 1742 nm developed for sensitive detection of hydrogen chloride (HCl)[38]. We periodically operate in CRDS mode to measure the decay time and infer the mirror reflectivity (as it is needed in the analysis) but Kerr measurements are made by sweeping the laser over cavity resonances

without extinguishing the beam. The system uses a commercially available distributed feedback (DFB) laser as the light source. The DFB lasers employ internal Bragg gratings to enable narrow linewidth single-frequency output and continuous (mode-hop free) tuning *without* the need for an external cavity. Therefore, the design is simpler and has fewer moving parts compared to an external cavity system in which the laser is tuned via a moving diffraction grating. The DFB laser we use (NEL model KELD1F5DAAA) has an output power of 15 mW, linewidth of ~5 MHz and a fiber coupled single-mode output. A schematic diagram of the optical aspects of the sensor is shown in Figure 24. The laser output is delivered to the optical cavity via several mirrors. The optical cavity has length of 90 cm and is formed by a pair of high reflectivity mirrors each 2.54 cm in diameter with reflectivity of 0.99998 (Advanced Thin Films). Simple beam-shaping optics (lens pair) are used to mode-match the beam to the cavity. During a typical experiment the laser is scanned (with a triangular current ramp) with a scan speed of 5.7 GHz/s over an extent of ~10 GHz such that it sequentially overlaps multiple cavity resonances. As described below, as the laser passes each resonance light is transmitted through the cavity and a trigger circuit (connected to the photodetector that monitors the parallel polarizer beam) is used to capture the signals through the two polarizers.

The applied electric field is created between a pair of parallel plates surrounding the cavity. The separation between the plates is 16 mm and they are connected to a high voltage DC power supply with applied voltages ranging from 0 to 18 kV. The sample gas flows slowly within a Pyrex tube that itself is between the parallel plates. The Pyrex tube is a dielectric that slightly alters the electric field. We have used a simple finite element solver and find that, for our geometry, the field in the tube is approximately 97% of the field found as the plate separation divided by the applied voltage (and we enter the fields into our model accordingly). We use a

thin film polarizer (Thorlabs LPNIR050-MP) to set the light polarization prior to entering the cavity. The polarization is set to an angle of 45 degrees relative to the electric field direction. A second analyzer polarizer (Glan-Taylor Thorlabs GT10-C) is positioned behind the cavity and is aligned to its null position (orthogonal to the input polarization). The Kerr induced polarization rotation causes the input linear polarization to become slightly elliptical so that a small fraction of the beam is transmitted through the analyzer. The transmitted beam is measured with an extended-wavelength InGaAs photodetector (Hamamatsu, G8421-03) with transimpedance amplifier (Analog Modules, 341-1-INV-10pF). In order to trigger and detect this rather weak beam, and to normalize laser power fluctuations, we also detect the (stronger) beam that is rejected by the analyzer polarizer (polarization approximately parallel to the input polarizer) with a second detector (Thorlabs PDA10CS). The signals from both photodetectors are passed to a computer via an A/D board (National Instruments, PCI-6132). The beam that is rejected by the polarizer is used to trigger the acquisition of signals from both beams. A pre-trigger (1.67 ms) is used in order to capture waveforms from each detector similar to those shown in Figure 23. The acquisition system averages multiple signals together (for each beam) as the laser passes repeatedly over the cavity resonance, and then fits an area (to the signal from each beam) and ratios these to one another.

To determine the ring-down time, we operate in CRDS mode (not shown in Figure 24) by removing the analyzer polarizer and using the extended-wavelength InGaAs photodetector to measure ring-down decays. In this case a triggering circuit (connected to the photodetector) monitors the cavity transmission and, as soon as the transmitted intensity reaches a pre-set threshold, triggers an acousto-optic modulator to extinguish the beam. The optical intensity within the cavity then decays (rings-down).

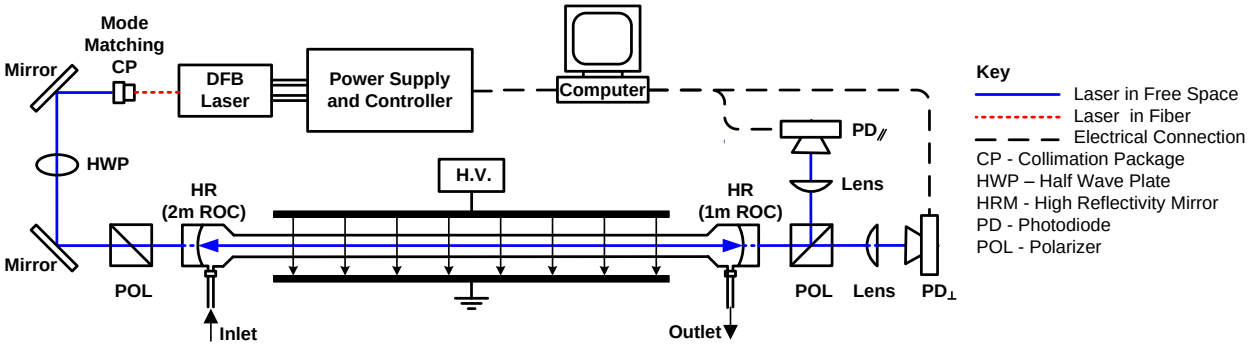

Figure 24 Schematic of cavity enhanced polarimeter with High Voltage plates.

3.2.1 OBSERVATION OF KERR INDUCED PHASE SHIFT AND TEMPORAL TRACES

Here, we present results illustrating the measurement system and the Kerr induced phase shift. Figure 25 shows traces through both polarizers (i.e., through the nulled polarizer that is perpendicular to the incident field, and through the aligned polarizer that is parallel to the incident field) for zero field and applied field cases. The sample gas in the cell is CO_2 at atmospheric pressure (0.85 bar in Fort Collins, CO). The temporal traces correspond to the signals measured on the two detectors as the laser is swept over cavity resonances. Individual traces, particularly for the perpendicular analyzer, are rather weak and the traces shown are averages (accumulations) of 6000 shots. Owing to the amplitude fluctuations of the individual shots, and the trigger method (fixed threshold), the averaging serves to temporally smear the individual traces so that their temporal extent is considerably broader than that predicted by the model (e.g. the modeled traces of Figure 23).

We first consider the left plots where there is no applied field. In this case, there is no Kerr induced polarization rotation and so light leaving the cavity is predominantly parallel to the

incident light. The signal on the parallel polarizer is therefore much larger than that of the perpendicular polarizer. The vertical scales for the two polarizers are different, owing to different detectors, but we have performed a calibration that shows that with zero field the total amount of light on the perpendicular polarizer is $1/400^{th}$ of the light on the parallel polarizer. Actually, the signal through the perpendicular polarizer should be nominally zero in this case but there is some light leakage which provides a background signal level that must be subtracted. The origin of the light leakage will be discussed in Section 3.3.1 but is primarily due to birefringent effects of the cavity mirrors. The plots on the right side show the corresponding traces but with an applied field of E = 9.87 kV/cm. In this case, the Kerr induced polarization rotation causes phase change between the electric field components parallel and perpendicular to the field, such that more signal is present through the perpendicular analyzer. The larger signal on the perpendicular analyzer with field on relative to field off clearly shows the signal due to the Kerr effect. Because the polarization ellipticity introduced by the Kerr effect is relatively weak, the signal through the parallel polarizer is relatively unchanged. Our measurement approach, as shown in the next sub-section, is to take the ratio of the area of the signal from the perpendicular analyzer to the area of the signal from the parallel analyzer. (From this ratio, we subtract the ratio of the corresponding traces with field off as a means to subtract the background.) In order to confirm that our signals are not due to some form of electromagnetic interference, we have performed a control test where we have positioned the parallel plates slightly away from the sample tube and we have seen no Kerr signal in this case.

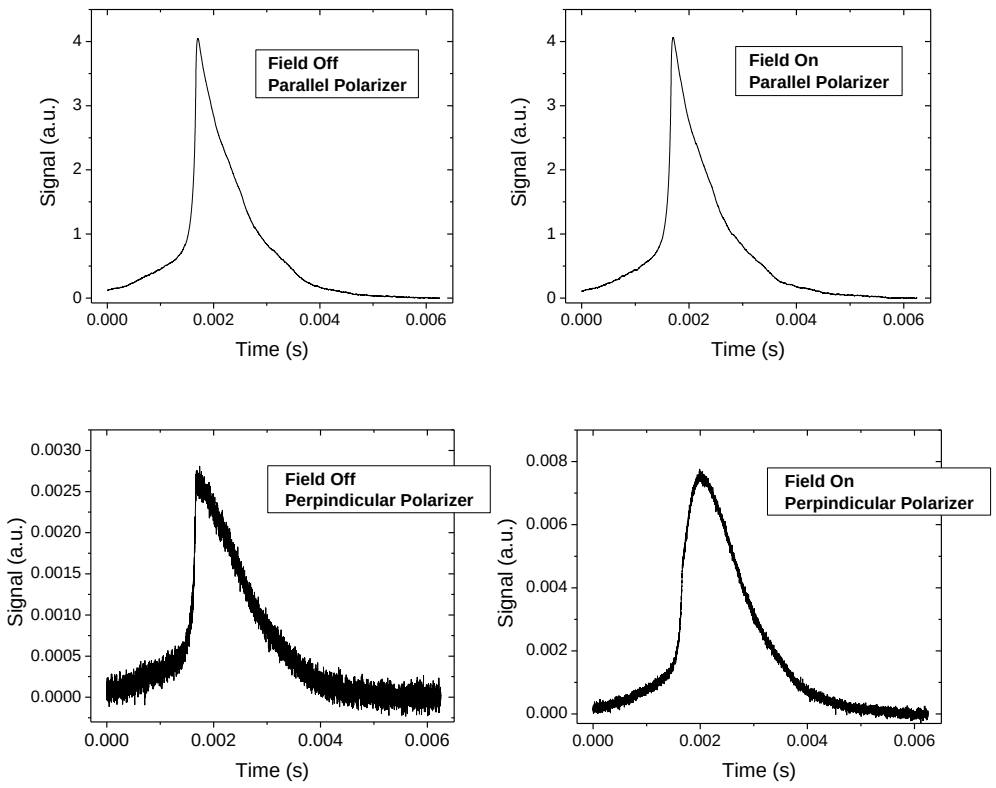

Figure 25 Illustrative Kerr signals due to CO_2 at atmospheric pressure from cavity enhanced polarimeter. Top left: Field off, parallel polarizer. Bottom left: Field off, perpendicular polarizer. Top right: Field on, parallel polarizer. Bottom right: Field on, perpendicular polarizer.

3.3 KERR EFFECT IN DIFFERENT GASES

In this subsection we show polarimeter results for several sample gases and compare against model predictions. Modeling was similar to that discussed in connection with Figure 23. We have simulated the temporal traces for the perpendicular and parallel analyzer orientations and determined the corresponding area ratio. The simulation conditions are as follows: λ=1742 nm, L_0 = 0.9 m, R = 0.999982 (corresponding to τ_{cav} = 166.7 μs and F = 174,000), v =

4.81μm/s (or equivalent laser scan speed of 5.8 GHz/s though Kerr ratios are quite insensitive to this parameter), and L = 0.55 m. The electric fields are computed based on the parallel plate separation, power supply voltage, and correction factor for the dielectric tube (as discussed above). Figure 26 shows experimental results for atmospheric pressure gases of CO_2, N_2, O_2, and air, while Figure 27 shows CO_2 at pressure of 2.9 atm. The plotted Kerr signal is the ratio of the (temporally integrated) light through the perpendicular polarizer to the light through the parallel polarizer. The background leakage signal has been subtracted from the measurements. For the model, we have used the following wavelength-independent Kerr constants: K_{CO_2} = 2.08x10^{-24} m^2/V^2 from [31], K_{O_2} = 4.19x10^{-25} m^2/V^2 from [36] (denoted Carusotto) and K_{O_2} = 6.58x10^{-25} m^2/V^2 from [31] (denoted Inbar), K_{N_2} = 1.92x10^{-25} m^2/V^2 from [36] (denoted Carusotto) and K_{N_2} = 2.65x10^{-25} m^2/V^2 from [31] (denoted Inbar), $K_{air} = 0.79K_{N_2} + 0.21K_{O_2}$. The aforementioned values are all for atmospheric pressure (1 atm) and we are assuming a linear scaling for number density and pressure (all measurements are at temperature of 293 K) [34]. The experimental error bars are determined from the system sensitivity and (observed) variation of light leakage level (see below).

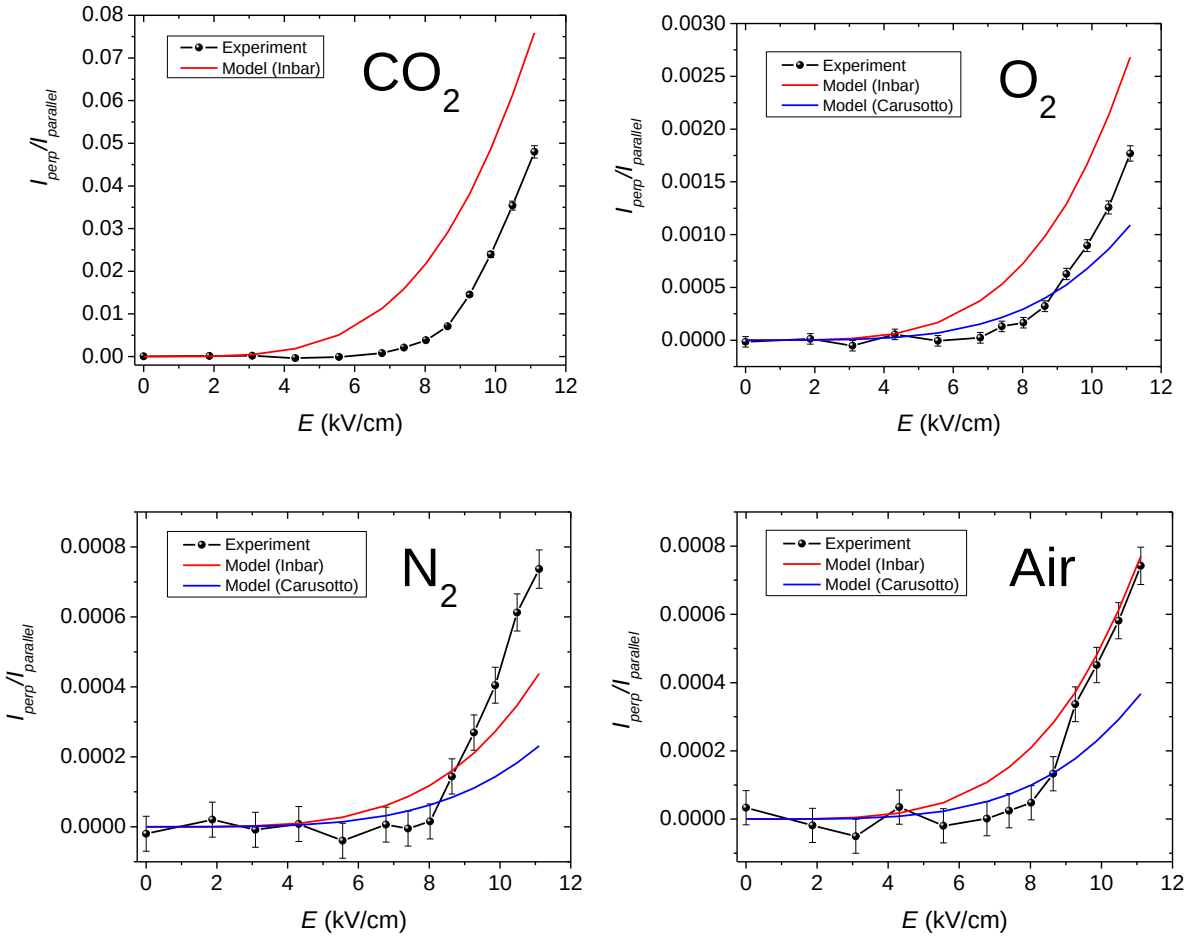

Figure 26 Kerr signal versus applied field for atmospheric pressure CO_2 (top left), O_2 (top right), N_2 (bottom left), and air (bottom right). The Kerr signal is the ratio of the (temporally integrated) light through the perpendicular polarizer to the light through the parallel polarizer.

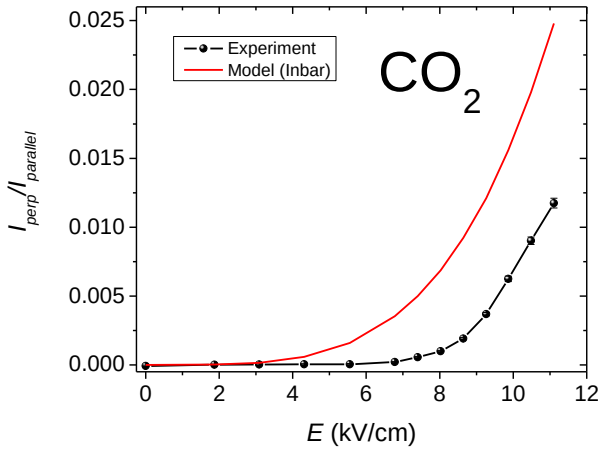

Figure 27 Kerr signal versus applied field for CO_2 at pressure of 2.9 bar. The Kerr signal is the ratio of the (temporally integrated) light through the perpendicular polarizer to the light through the parallel polarizer.

The CO_2 molecule has a large Kerr constant and signal relative to the other gases studied. In our measurement system its signal is evident for fields exceeding ~7 kV/cm. The Kerr constants for N_2 and O_2 are relatively weaker with resulting smaller Kerr signals. The agreement between model and experiment is generally rather good given the uncertainty in the Kerr constants, for example, even for the relatively large constant for CO_2, Inbar et al report an uncertainty of 30% [31] which then becomes consistent with experiment. Another effect, discussed below, that may explain the difference of model versus experiment is laser linewidth effects.

3.3.1 LASER LINEWIDTH EFFECTS

Although the linewidth of our DFB laser is relatively small, its effect on the measurements should be considered. It is known that laser linewidth (phase noise) influences the

power injection to high-finesse cavities and can alter ring-down and CEAS signals. A particular effect, prevalent when exciting a high-finesse cavity, is that the frequency selective nature of the cavity serves to convert laser phase-noise to power amplitude fluctuations. The amplitude fluctuations, as discussed below, are a limiting factor in the sensitivity of our system. We have also quantitatively examined the effect of laser linewidth on the signals (through the parallel and perpendicular analyzer polarized) in our experiment. For this analysis, we use expressions from Morville et al. that are similar to equations (13) and (14) but that include random walk due to laser phase noise [37]. (The expressions we use are based on eqn. (12) of the Morville publication though we have fixed an error of inconsistent dimensions.) We have considered cases for N_2 and CO_2 for applied fields of 8.5 kV/cm and we have assumed a (short term) laser linewidth of 100 kHz. For each of the cases we have run 300 simulations (each seeded with different random phase fluctuations) and looked at the mean ratio. We find that, in comparison to equations (13) and (14) which is for a monochromatic laser, the ratio of the areas due to the perpendicular and parallel signals changes by a fractional value of less than 1 part in 10. However, we have not measured our actual laser linewidth and higher linewidths will give larger signal reductions. This issue should be further considered and is not incorporated within the current analysis.

3.3.2 SENSITIVITY AND DETECTION LIMITS

The detection limit of our instrument is due to the precision with which we can measure the ratios of the perpendicular to parallel light signals. For our measurement configuration (6000 shot averages) and the case of no applied field, the smallest measurable (change of) signal

intensity ratio is ~5x10^{-5} (50 ppm). For example, repeated measurements of the background leakage signal (which we assume to be stable) yield 0.00250 ± 0.00005. A similar conclusion is found by looking at the signal variation for low field conditions in Figure 25. We have verified with our model that, for rough calculations, one can relate the per-pass Kerr phase change to the analyzer intensity ratio by using equation (10) and introducing the cavity enhancement factor:

$$\frac{I_0}{I_i} \approx \sin^2\left(\frac{2F}{\pi}\frac{\theta_K}{2}\right) \tag{15}$$

In this case we use I_0/I_i should be interpreted analogously as the ratio of the light through the perpendicular polarizer to parallel polarizer, i.e. to the quantity plotted on the ordinate axis of Figure 26 and Figure 27. (In fact, for sufficiently weak birefringence, equation (15) gives the correct intensity ratio very accurately if one also introduces a multiplier of 0.5.) Using equation (15) with a minimum measurable I_0/I_i of 5x10^{-5} yields, for our conditions, a minimum measurable per-pass Kerr phase change of 0.2 μradians. In comparison to the work of Kumada et al., who used an optical cell and electrode length of 1.3 m in a 10-pass configuration, we have achieved a lower minimum measurable phase change by a factor of approximately 250. In terms of using our diagnostic for studying plasmas in atmospheric pressure air, the current system allows measurements of fields of $E \approx 7$ kV/cm for our 55 cm length electrodes which would correspond to field amplitudes of approximately 15 kV/cm and 50 kV/cm for shorter field lengths of 10 cm and 1 cm respectively. These sensitivities are within range of the field strengths seen in the cathode fall of direct current glow discharges[32],[33], and suggest that this CRDP measurement might be a useful method for probing the field strength in the sheaths of discharge

plasmas. Such a diagnostic could be useful in characterizing the field from a wire to plate corona discharge, with the laser propagating along the length of the long wire electrode [39]. The effects of beam steering introduced by index-of-refraction variations associated with candidate plasmas should also be considered in future work.

4. CONCLUSIONS AND FUTURE WORK

This thesis described the development of two non-intrusive laser diagnostic techniques with applications to electric propulsion and plasma research. The work on xenon ion laser-induced fluorescence shows significant progress toward sheath profile measurement via Xe+ velocimetry with a focus towards quantification of the plasma density detection limit. An optical noise study determined that significant reduction of plasma and filament luminosity is crucial for plasma sheath detection at lower plasma density. This study also showed that sheath measurements may be possible at current plasma density conditions if magnification imaging could be implemented to reduce the spatial resolution of the measurement sufficiently to resolve very thin sheaths.

The work on cavity enhanced polarimetry described successful demonstration of electric field measurements via the optical Kerr effect with significant improvement in detection limit compared to similar research. The data gathered using the instrument shows generally good agreement between model and experiment considering large uncertainty related to the Kerr constants used for modeling. The sensitivity of the instrument in its current configuration falls within the range of field strengths seen in DC glow discharge plasma sheaths and could be used in some plasma applications. Further research is necessary to improve instrument sensitivity for more versatile operation with broader plasma applications.

4.1 FUTURE WORK FOR XE+ LIF

A significant amount of work is still necessary to obtain accurate sheath potential profiles using the LIF apparatus described in chapter 2 at the current SNR and spatial resolution.

Once these spatially resolved IVDF profiles have been recorded, work must also be completed on the accurate interpretation and calculation of plasma potential curves using the IVDF information; such calculations have not been fully studied as of yet due to lack of meaningful data. Ultimately, the technique developed in this research will be implemented into plasma discharge sources that will be designed by University of Michigan researchers to exhibit significant secondary electron emission from the target material. There are several major improvements to the current LIF apparatus and procedure that must occur to achieve these goals and will be discussed in this section.

All of the areas of future work proposed in this section relate to increasing the SNR of the system to facilitate measurement of sheaths. Decreasing the contribution of the filament and plasma luminosity to the noise of the IVDF measurement will be crucial to the ability of this system to accurately map plasma sheaths at lower densities. Our affiliates at UM have proposed implementation of baffling in the plasma source to limit the direct line of sight path that filament luminosity and have shown preliminary testing of such baffling which reduced the filament luminosity out of the collection windows on the discharge source canister by roughly 50%. Implementation of another electron source in place of the filament with greatly reduced luminosity emission, such as hollow cathodes or plasma bridge neutralizers, could potentially reduce the luminous noise greatly without the need for a baffling apparatus.

As discussed in section 2.3, SNR can be increased through averaging of the LIF signal over many wavelength scans but improves as the square root of the number of averages. That method of noise reduction requires nearly 90 minutes of data gathering for a SNR increase of 5. In recent tests, the plasma discharge current has been observed to drift of extended periods of time, which leads to a concern of the stability of the plasma over these time periods. If there is a

significant drift of plasma parameters during a 90 minute test, the 25 trace averages no longer represent an accurate measurement. It would therefore be more advantageous to achieve SNR improvement through operation at higher LIA time constants. As discussed in section 2.2.2, the scan range required to obtain both the LIF and galvatron features in the same scan sets a minimum scan speed based on the slowest laser scan frequency allowed by the laser controller. This scan speed limit requires the LIA be operated at a sufficiently short time constant (100 ms) in order to deter artificial frequency shifting of the feature while still filtering as much noise as possible. Increasing the time constant from the current 100 ms setting to a 300 ms setting could potentially improve the SNR by a factor of 3 over a single 200 s scan rather than requiring 9 scans to achieve the same improvement using averaging. This scan range reduction and time constant increase would still allow for increased SNR with the same 200 s scan period used in the current procedure. This would reduce measurement time for a given SNR and therefore limit the affects of long-term plasma density drift during measurement procedures.

This improvement, however, presents several difficulties that must be worked around if such a change were to be made. The scan range limitation discussed in section 2.2.2 is set by the need for the absolute wavelength reference provided by the galvatron. The galvatron work thus far has not proven successful in finding an opto-galvanic signal at the same transition as is used in the LIF procedure. An in-depth study of the galvatron operation and the components (ballast resistor capacitor, chopping frequency, operating voltage, etc.) used in its circuitry could potentially reveal operating parameters which allow for detection of the 834.954 nm xenon ion transition.

If such an alteration in operational parameters cannot be found to use the galvatron in this way, other means of absolute wavelength determination may need to be explored. If a neutral

gas-phase species can be found with a strong absorption line closer to the LIF transition than the neutral xenon transition currently used with the galvatron, a single pass absorption method could potentially replace the galvatron for absolute wavelength reference.

Regardless of the success of the previously described SNR improvements, work must be conducted to improve the spatial resolution of the LIF collection configuration. As discussed in section 2.3, the operation of the plasma source exhibits far higher densities than previously assumed. The test data for the plasma discharge source during argon operation fueled apparatus designs based on sheath thicknesses on the order of several millimeters to centimeters. Even if the work described earlier in this section does result in significant noise reduction and SNR improvement, the plasma sheath will still be much thicker than the current imaging and collection system is capable of resolving. Increasing the magnification of the imaging setup as well as reduction of the entrance slit of the monochromator would allow for a smaller detection volume to be collected and therefore create a finer spatial resolution for the IVDF measurements. As discussed in section 2.3, The spatial resolution of the LIF collection must be less than the Debye length to allow for roughly 10 potential measurements to be made within the plasma sheath. At the current SNR limits, the magnification of the collection optics would need to be increased to 8:1 in order to resolve sheaths at $n_i \sim 5 \cdot 10^{11}$ cm^{-3}. To be able to compare potential measurements using LIF methods with probe measurements to verify the accuracy of the technique, however, it is necessary to improve the detection sensitivity to 10^9 -10^{10} cm^{-3} where accurate probe measurements can be taken.

Additional noise reduction could possibly be achieved through blocking of the entrance slit above and below the imaged fluorescence column along the beam path to stop any extra filament of plasma luminosity (not within the desired collection volume) from entering the

monochromator. Tests are currently being conducted to determine the effectiveness of this process and quantify any noise reduction.

4.2 FUTURE WORK FOR CAVITY ENHANCED POLARIMETRY

More experimental characterization is needed to understand the physical origin of our detection limit. For example, in terms of pure length enhancement, our effective electrode length is ~50 km, which is ~4000 times longer than that of Kumada et al., meaning we could expect roughly another order of magnitude sensitivity improvement. Factors which also play into our sensitivity limit include possible variation in the cavity background birefringence as well as detector noise and shot noise (particularly for the perpendicular analyzer leg) where the optical power is low and we use an uncooled extended wavelength InGaAs detector. Better performance may be achieved by changing to a lower laser wavelength where more sensitive (regular InGaAs) detectors can be used and, assuming truly wavelength-independent Kerr constants, higher phase shifts arise for given field conditions.

For measurements of very weak phase shifts the birefringent nature of the optical cavity itself should be considered [40]. We have observed that our light leakage signal is due predominantly to the optical cavity and not to the suppression of our polarizers. The observed light leakage of ~0.0025 corresponds to a phase change of ~1 μradians per mirror per pass which is approximately consistent with measured values [40], [41]. If the cavity mirror acts as a pure (and stable) waveplate then, as we have done, its phase contribution can be subtracted as a background, but as discussed by Huang et al. optical cavities can also exhibit linear dichroism (polarization dependent loss). While they may be less useful for practical plasma

implementations several recent publications have considered more complex locked and modulated schemes that allow measurements of smaller phase shifts [41], [42].

REFERENCES

[1] D. M. Goebel and I. Katz, "Fundamentals of Electric Propulsion: Ion and Hall Thrusters." 2008.

[2] R. A. Gulczinksi, F.S. and Spores, "Analysis of Hall-Effect Thrusters and Ion Engines for Orbit Transfer Missions," in *AIAA Joint Propulsion Conference*, 1996.

[3] F. F. Chen, *Introduction to Plasma Physics and Controlled Fusion*, 2nd ed. Springer, 1984, 2006, pp. 290–295.

[4] A. Dunaevsky, Y. Raitses, and N. J. Fisch, "Secondary electron emission from dielectric materials of a Hall thruster with segmented electrodes," *Physics of Plasmas*, vol. 10, no. 6, p. 2574, 2003.

[5] J. M. Elizondo, K. Meredith, and N. Lapetina, "Ceramic secondary electron emission and surface charge measurements," *IEEE Transactions on Plasma Science*, vol. 30, no. 5, pp. 1955–1960, Oct. 2002.

[6] N. Hershkowitz, "Sheaths: More complicated than you think," *Physics of Plasmas*, vol. 12, no. 5, p. 055502, 2005.

[7] W. Huang, "Study of Hall Thruster Discharge Channel Wall Erosion via Optical Diagnostics," University of Michigan, 2011.

[8] D. Lee, N. Hershkowitz, and G. D. Severn, "Measurements of Ar+ and Xe+ velocities near the sheath boundary of Ar–Xe plasma using two diode lasers," *Applied Physics Letters*, vol. 91, no. 4, p. 041505, 2007.

[9] W. Li, J. X. Ma, J. Li, Y. Zheng, and M. Tan, "Measurement of virtual cathode structures in a plasma sheath caused by secondary electrons," *Physics of Plasmas*, vol. 19, no. 3, p. 030704, 2012.

[10] Y. Raitses, a. Smirnov, D. Staack, and N. J. Fisch, "Measurements of secondary electron emission effects in the Hall thruster discharge," *Physics of Plasmas*, vol. 13, no. 1, p. 014502, 2006.

[11] Y. Raitses, D. Staack, M. Keidar, and N. J. Fisch, "Electron-wall interaction in Hall thrusters," *Physics of Plasmas*, vol. 12, no. 5, p. 057104, 2005.

[12] E. Sternglass, "Theory of secondary electron emission by high-speed ions," *Physical Review*, vol. 108, no. 1, pp. 1 – 12, 1957.

[13] F. Taccogna, S. Longo, and M. Capitelli, "Effects of secondary electron emission from a floating surface on the plasma sheath," *Vacuum*, vol. 73, no. 1, pp. 89–92, Mar. 2004.

[14] A. D. Gallimore and L. Wang, “An Investigation of Plasma-Wall Interactions in Plasma Propulsion Systems.” p. 7, 2011.

[15] J. P. Sheehan and N. Hershkowitz, “Negative plasma potential in a multidipole chamber with a dielectric coated plasma boundary,” *Journal of Vacuum Science & Technology A: Vacuum, Surfaces, and Films*, vol. 30, no. 3, p. 031302, 2012.

[16] F. F. Chen, “Electric Probes,” in in *Plasma Diagnostic Techniques*, 1st ed., R. H. Huddlestone and S. L. Leonard, Eds. New York: Academic Press, 1965, pp. 113–200.

[17] L. Oksuz and N. Hershkowitz, “Negative plasma potential in unmagnetized DC electropositive plasma with conducting walls,” *Physics Letters A*, vol. 375, no. 22, pp. 2162–2165, May 2011.

[18] G. Bourgeois, S. Mazouffre, and N. Sadeghi, “Unexpected transverse velocity component of Xe+ ions near the exit plane of a Hall thruster,” *Physics of Plasmas*, vol. 17, no. 11, p. 113502, 2010.

[19] D. Gawron, S. Mazouffre, N. Sadeghi, and a Héron, “Influence of magnetic field and discharge voltage on the acceleration layer features in a Hall effect thruster,” *Plasma Sources Science and Technology*, vol. 17, no. 2, p. 025001, May 2008.

[20] A. D. Buckingham and D. A. Dunmur, “Kerr effect in inert gases and sulphur hexafluoride,” *Transactions of the Faraday Society*, vol. 64, p. 1776, 1968.

[21] W. Huang, B. M. Reid, T. B. Smith, and A. D. Gallimore, “Laser-Induced Fluorescence of Singly-Charged Xenon in a 6-kW Hall Thruster Plume,” in *AIAA Joint Propulsion Conference*, 2008, no. July, pp. 1–14.

[22] C. W. Bruce, “Electro-optical Kerr effect in gases,” *Physical Review*, vol. 44, pp. 682–686, 1933.

[23] W. Breazeale, “The electro-optical Kerr effect in ammonia, nitrogen and oxygen,” *Physical Review*, vol. 48, pp. 237–240, 1935.

[24] A. Kumada, A. Iwata, K. Ozaki, M. Chiba, and K. Hidaka, “Kerr effect in gas and its application to noncontact measurement of electric field,” *Journal of Applied Physics*, vol. 92, no. 5, p. 2875, 2002.

[25] T. Müller, K. Wiberg, and P. Vaccaro, “Cavity ring-down polarimetry (CRDP): a new scheme for probing circular birefringence and circular dichroism in the gas phase,” *The Journal of Physical Chemistry A*, vol. 104, pp. 5959–5968, 2000.

[26] K. B. Wiberg, P. H. Vaccaro, T. Mu, J. R. Cheeseman, and M. J. Frisch, “Cavity ring-down polarimetry (CRDP): theoretical and experimental characterization,” vol. 19, no. 1, pp. 2–5, 2002.

[27] R. Engeln, G. Berden, E. van den Berg, and G. Meijer, “Polarization dependent cavity ring down spectroscopy,” *The Journal of Chemical Physics*, vol. 107, no. 12, p. 4458, 1997.

[28] R. Engeln, G. Berden, R. Peeters, and G. Meijer, “Cavity enhanced absorption and cavity enhanced magnetic rotation spectroscopy,” vol. 69, no. 11, pp. 3763–3769, 1998.

[29] M. Mansuripur, “Reciprocity in Classical Linear Optics,” *Optics and Photonics News*, no. July, pp. 53–58, 1998.

[30] F. Bielsa, R. Battesti, C. Robilliard, G. Bialolenker, G. Bailly, G. Trénec, a. Rizzo, and C. Rizzo, “Kerr effect of molecular oxygen at λ=1064 nm,” *The European Physical Journal D*, vol. 36, no. 3, pp. 261–269, Aug. 2005.

[31] E. Inbar and A. Arie, “High-sensitivity measurements of the Kerr constant in gases using a Fabry–Perot-based ellipsometer,” vol. 852, pp. 849–852, 2000.

[32] H. Shan, S. A. Self, and M. A. Capelli, “Optical Emisison-Based Measurements of Electric Field in the Cathode Fall Region of He and CF4/He DC Glow Discharges,” in *44th Annual Gaseous Electronics Conference*, 1991.

[33] Y. W. Choi, M. D. Bowden, and K. Muraoka, “Electric field measurements in an argon glow discharge using laser spectroscopy,” *Applied Physics Letters*, vol. 69, no. 10, p. 1361, 1996.

[34] D. Chauvat, A. Le Floch, M. Vallet, and F. Bretenaker, “Cotton–Mouton effect measurement with the Fabry–Perot eigenstates,” *Applied Physics Letters*, vol. 73, no. 8, p. 1032, 1998.

[35] F. Brandi, F. Della Valle, and P. Micossi, “Cotton – Mouton effect of molecular oxygen : a novel measurement,” vol. 15, no. 4, pp. 1278–1281, 1998.

[36] S. Carusotto, E. Iacopini, E. Polacco, and F. Scuri, “Measurement of the kerr constant of He, A, O 2, N 2, H 2 and D 2,” *Il Nuovo Cimento*, vol. 5, no. 4, pp. 328–338, 1985.

[37] J. Morville, D. Romanini, M. Chenevier, and A. Kachanov, “Effects of laser phase noise on the injection of a high-finesse cavity.,” *Applied optics*, vol. 41, no. 33, pp. 6980–90, Nov. 2002.

[38] C. L. Hagen, B. C. Lee, I. S. Franka, J. L. Rath, T. C. VandenBoer, J. M. Roberts, S. S. Brown, and a. P. Yalin, “Cavity ring-down spectroscopy sensor for detection of hydrogen chloride,” *Atmospheric Measurement Techniques Discussions*, vol. 6, no. 4, pp. 7217–7250, Aug. 2013.

[39] P. Bérard, D. A. Lacoste, and C. O. Laux, “Corona Discharges in Atmospheric Air Between a Wire and Two Plates,” vol. 39, no. 11, pp. 2248–2249, 2011.

[40] H. Huang and K. K. Lehmann, “Effects of linear birefringence and polarization-dependent loss of supermirrors in cavity ring-down spectroscopy.,” *Applied optics*, vol. 47, no. 21, pp. 3817–27, Jul. 2008.

[41] M. Durand, J. Morville, and D. Romanini, “Shot-noise-limited measurement of sub–parts-per-trillion birefringence phase shift in a high-finesse cavity,” *Physical Review A*, vol. 82, no. 3, Sep. 2010.

[42] J. Morville and D. Romanini, “Sensitive birefringence measurement in a high-finesse resonator using diode laser optical self-locking,” *Applied Physics B: Lasers and Optics*, vol. 74, no. 6, pp. 495–501, Apr. 2002.